USING INFRARED SPECTROSCOPY TO ASSESS PALEOFLUID FLOW CHARACTERISTICS OF CLAY GOUGE OF THE MOAB FAULT, UT

by

Paula Fleischmann

APPROVED BY SUPERVISORY COMMITTEE:

____________________________________________

Tom Brikowski, Chair

____________________________________________

John W. Geissman

____________________________________________

Lowell Waite

USING INFRARED SPECTROSCOPY TO ASSESS PALEOFLUID FLOW CHARACTERISTICS OF CLAY GOUGE OF THE MOAB FAULT, UT

by

PAULA FLEISCHMANN, BS

THESIS

Presented to the Faculty of

The University of Texas at Dallas

in Partial Fulfillment

of the Requirements

for the Degree of

MASTER OF SCIENCE IN

GEOSCIENCE

THE UNIVERSITY OF TEXAS AT DALLAS
May 2022

ACKNOWLEDGMENTS

I would first like to give my appreciation to my thesis advisor, Dr. Brikowski, for his guidance and dedication throughout this thesis project. I also want to thank my committee members Dr. John Geissman and Lowell Waite for their review of this thesis, mentorship, and encouragement throughout my graduate education. I would then like to thank my fellow colleagues Dr. Ann Moulding, Siloa Willis, and Kaitlyn Stacey assisting me with field work in Moab, Utah whilst having a great time in the Wild West, and my dear Samuel P. Johnson for his aid and support while I was writing this thesis. Additionally, I'd like to acknowledge my appreciation for the acquaintances I made in Moab, Doug Sprinkel from the Utah Geologic Survey and my dear friend Cassidy Walker. Furthermore, I'd like to acknowledge and thank the employees of Jenn's Jeep Rentals in Moab, Utah for giving me a great deal for renting a brand new, tricked out, off-road Jeep for adventuring out to my field sites. Finally, I'd like to thank the most important people in my life: my parents.

"*There is no vestige of a beginning, no prospect of an end.*" ~ James Hutton, 1788

"*Much as I admired the elegance of physical theories, which at that time geology wholly lacked, I preferred a life in the woods to one in the laboratory.*" ~ John Tuzo Wilson, 1982

February 2022

USING INFRARED SPECTROSCOPY TO ASSESS PALEOFLUID FLOW CHARACTERISTICS OF CLAY GOUGE OF THE MOAB FAULT, UT

Paula Fleischmann, MS
The University of Texas at Dallas, 2022

Supervising Professor: Dr. Tom Brikowski

The origin, continuity, and mineralogy of fault gouge is crucial for determining the potential degree of fault seal formation. Of particular interest is the role of fluids in gouge formation. These issues have broad applicability in petroleum geology, underground waste disposal, carbon sequestration, and more. The Moab Fault in Utah is a classic example of a sedimentary basin-bounding normal fault complex in a salt-related petroleum system with abundant gouge, and spectral signatures of its gouge may be indicative of past fluid flow events and related formation of clay minerals. The Terraspec Halo, a "quantitative reconnaissance" tool and infrared mineral identifier, was applied to exposures of clay gouge at three locations along the 45 km long Moab Fault to assess the nature and origin of the gouge. The method consists of measuring profiles of infrared spectra and scalar values in close spacing across the fault plane and damage zone, extending into the adjacent wall rock. Absorbance peak locations (e.g., Al-OH absorption feature of clay minerals), help indicate geochemical conditions during mineral formation or alteration. This combination of spectral features can be diagnostic of diagenetic vs. hydrothermal origins for clay minerals. Minerals identified include smectite, magnesium and potassium illite, montmorillonite, hematite, malachite, phengite, and goethite. Carbonate, silica, and copper mineralization in the core and damage zone of two of the sites along the fault suggests significant post-faulting low-temperature fluid movement. Spectral indicators of mineral maturity (e.g., Illite Spectral Maturity or ISM) help gauge the temperature of hydrothermal alteration events. Results suggest a distinctly lower ISM in most of the clay gouge compared to surrounding bedrock. This indicates a significant component of low-temperature hydrothermal alteration and clay formation, and a major contribution of neo-formed clays to the gouge. Concordant with previous studies utilizing traditional, time and labor-intensive laboratory analysis, field analysis with the Terraspec Halo produced evidence for both low and high-temperature fluid migration events. Based on scans transecting wall rock and fault gouge, evidence exists which suggests that sections of the Moab fault acted as a seal in some areas and as a conduit for fluid flow in others. Whether the fault acts as a seal or conduit for fluids at a given site may depend on multiple factors, such as magnitude of displacement, juxtaposed lithologies at a given fault segment, characteristics of gouge material, and complex spatio-temporal paleofluid history.

TABLE OF CONTENTS

LIST OF FIGURES

LIST OF TABLES

# CHAPTER 1

# INTRODUCTION

Are faults conduits or seals? What are the factors that fluid interaction with faults? Hydraulic properties associated with faults are strongly dependent on the nature of their fault gouge (Caine et al., 1996; Haines & van der Pluijm, 2012), which determines whether a fault will act as a barrier or a conduit for fluid flow, as well as its frictional strength. Breakthroughs in understanding the genesis and mechanics of clay and shale smears, the primary contributors to gouge formed in sedimentary rocks, are crucial to the developments in many fields of study including mineral and hydrocarbon exploration geology (Davatzes & Aydin, 2005; Foxford et al., 1998; Garden et al., 2001; Pevear, 1999). The clay content in fault gouge zones is dictated by the amounts of wall-rock protolith derived (detrital) minerals and neoformed (authigenic) clay minerals resulting from fault or deformation related processes resulting in hydrothermal neocrystallization (Haines et al., 2009; Solum et al., 2005; Vrolijk & Van der Pluijm, 1999). The Moab Fault system in the Paradox Basin of Utah exposes several faults of different throw magnitudes, gouge thicknesses, and associated fluid migration features (Chan et al., 2000; Davatzes & Aydin, 2005; Davatzes et al., 2003; Eichhubl et al., 2009; Foxford et al., 1996, 1998; Johansen et al., 2005; Johansen & Fossen, 2008; Nuccio & Condon, 1996). These features make the Moab Fault an ideal feature for the examination of gouge development and the role of fluid migration in the area, and may help determine the presence of paleofluid flow and its potential effects on clay mineral alteration within the fault gouge.

## 1.1 Aim of Study

The goals within study are to gain a better understanding of the origin of clay minerals related to fluid-influenced alteration, and to utilize IR spectroscopy as an alternative, field-deployable aid in classifying fault gouge materials and deducing a fluid migration history**.** This is done by investigating the wall rocks and the fault gouge, which incorporates comminuted minerals from the fault hanging wall and foot wall rocks, as well as more recent authigenic clay minerals which formed directly by fluid interaction (Haines et al., 2009; Solum et al., 2005, 2010; Vrolijk & Van Der Pluijm, 1999). Previous studies of the nature of fault gouges have primarily relied on the labor-intensive X-ray diffraction (XRD) method, which is tedious and expensive regarding sampling and data processing. This study utilizes a field-portable infrared mineral identifier, which requires about one minute per sample analysis, vastly expanding the possible number of measurements to address the questions posed in this study.

## 1.2 Geologic Context

Large normal faults in the Paradox Basin of the Colorado Plateau are known to have experienced episodes of paleo-fluid during the Mesozoic to Cenozoic (Nuccio & Condon, 1996; Foxford et al., 1996, 1998; Chan et al., 2000; Davatzes et al., 2003, 2005; Johansen et al., 2005, 2008; Eichhubl et al., 2009). Faults may act as barriers or conduits to fluid migration, which usually occurs within and is determined by the physical properties of the fault gouge. Understanding the origin of the gouge, and how fluids subsequently modify it, is crucial to determining the behavior of the fault. Subtle mineralogic variations of clay minerals in fault gouge and damage zones may indicate alteration of detrital or neo-formed (authigenic) clays**.** A portable infrared spectral analyzer and mineral identifier is being used to assess fault gouge characteristics of the classic and extensively studied 45 km long, NW trending Moab Fault system located in the northern "Fold and Fault Belt" of the Paradox Basin (Fig. 1).

# CHAPTER 2

# GEOLOGIC SETTING

This study bears on the formation and evolution of the Moab Fault, along which displacement occurred throughout the Late Cretaceous and Cenozoic, in response to halokinetic movement and dissolution of underlying Pennsylvanian salt-bearing strata. Influential fluid migration along the fault likely began with early warm upwelling brines, supplanted by later, cool downflowing meteoric fluids, especially in the late Cenozoic. Secondary minerals and alteration features within the fault zone are a combination of comminuted or smeared wall rocks (e.g., Jurassic to Cretaceous clays) and younger authigenic minerals primarily influenced by fluids infiltration.

## 2.1 Regional Geology

The Moab Fault is within the “Fold and Fault Belt” (Nuccio and Condon, 1996.) of the Paradox Basin, in the central part of the Colorado Plateau (Fig 1). The well documented salt-related structures of the area were formed by regional tectonism and salt-influenced events (Doelling, 1988; Doelling & Baars, 2007; Doelling, 1985). During the Pennsylvanian and Permian periods, the Paradox Basin experienced simultaneous structural downwarping and uplift along its northeast border, which led to an accumulation of sediments. The evaporite rocks of the Pennsylvanian Paradox Formation were deposited in a series of cyclical repetitions of marine flooding and desiccation of a restricted shallow sea (Doelling, 1988; Nuccio and Condon, 1996).

Displacement along northwest-trending basement faults accommodated the basin subsidence (Foxford et al, 1996.) and the region was subject to multiple phases of salt tectonism. The most active salt movement occurred during the Pennsylvanian to Triassic and deformation of the Paradox Formation resulted in a series of NW-SE trending salt anticlines along the northeast margin of the basin. Throughout the Triassic to mid-Cretaceous, the salt anticlines continued to develop and thicken due to the localized salt movement from overburden deformation (Doelling, 1988), among other halokinetic mechanisms (Davidson et al., 1996). During a period of halokinetic quiescence, the salt structures were then buried by about 2km of post-Triassic sedimentary rocks. The influence of basement-involved faults coupled with local and regional extension related to salt dissolution along the crests of anticlines assisted in producing many salt-related structures (i.e. the Moab Valley). The Paradox Basin then experienced further modification during Cenozoic tectonic events. At about 37 Ma, the salt structures were exhumed due to uplift of the Colorado Plateau associated with young phases of the Sevier and Laramide orogenies (Foxford, 1996), then subsequently dissolved by groundwater, which led to collapse of salt-cored anticlines, resulting in the Moab and Lisbon Valley grabens (Chan et al., 2000; Nuccio & Condon, 1996). Some workers have proposed that Cenozoic volcanism associated with the La Sal Mountains volcanic center could have driven hydrothermal flow (Chan et al., 2001; Solum et al., 2010).

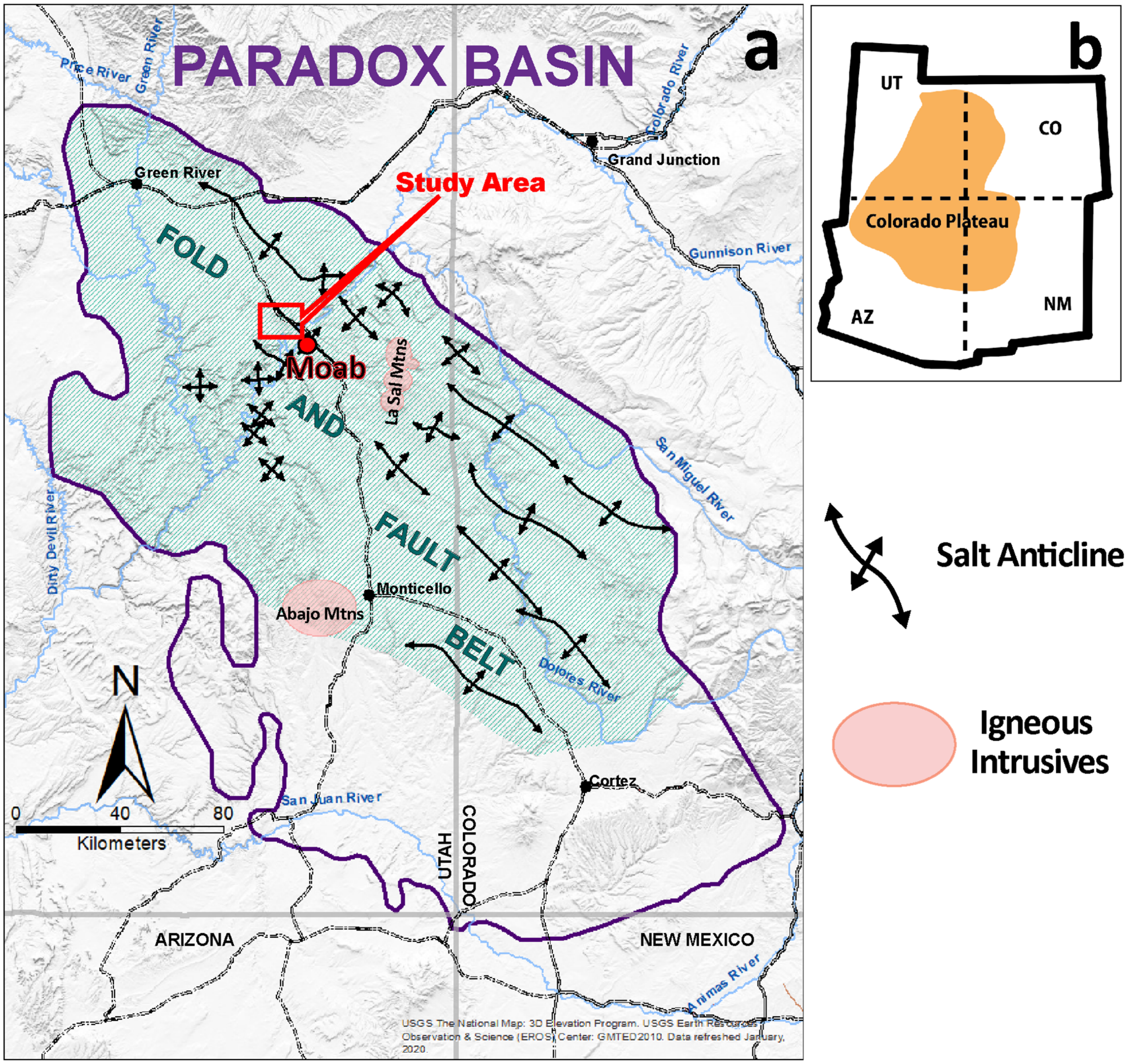


Figure 1. a) Map of the Fold and Fault Belt and salt anticlines in the Paradox Basin (purple outline), with geographic context. Red box outlines the Moab study area. Modified from Nuccio and Condon (1996). b) The Paradox Basin is located within the central part of the Colorado Plateau. For details on field sites and Moab fault structure, see Figure 3.

## 2.2 Moab Fault

The Moab Fault is a 45 km long trace NW trending complex normal fault system, well-exposed northwest from the city of Moab, offsetting a Pennsylvanian to Cretaceous sedimentary rocks (Foxford et. al., 1996) (Fig. 2). The main fault trace extends NW about 19 km from the city of Moab, subparallel to Hwy 191, then splays at the Courthouse branch point (Fig. 2b) for another 16km in a WNW trend, where it becomes a structurally diffuse fault zone. Structural complexities in that northern section include horsetail splays, extensional steps (Courthouse Branch point), fault intersections, separation of fault segments by relay zones, and fault terminations (Foxford et. al., 1998; Eichbul et. al. 2009). Lithologic juxtaposition between host rocks transitions northward from large fault throws near Moab to minor throws in the north, specifically Permian and Triassic redbed rocks against Upper Jurassic sandstone rocks to Jurassic rocks against Lower Cretaceous. In the northern splayed section of the Moab Fault, the minor splays juxtapose Jurassic against Cretaceous strata.

The fault's maximum vertical displacement (throw) in the Moab Canyon is about 1km (Foxford et. al., 1996), and is interpreted to have been caused by the collapse of Pennsylvanian and younger rocks into the dissolving core of the anticline. The Moab Fault experienced episodic movement, with the first phase of activity during the Permian-Triassic to early Jurassic time in response to salt tectonism from deposition of thick Permian and Triassic strata coupled with salt and fault movements (Foxford et al., 1996, 1998)A period of structural quiescence predated a second phase of post-mid-Cretaceous activity from Laramide age reactivated salt movement, which was active intermittently throughout the Cenozoic (Fig. 4; Foxford et. al. 1996, 1998; Chan et. al. 2000).

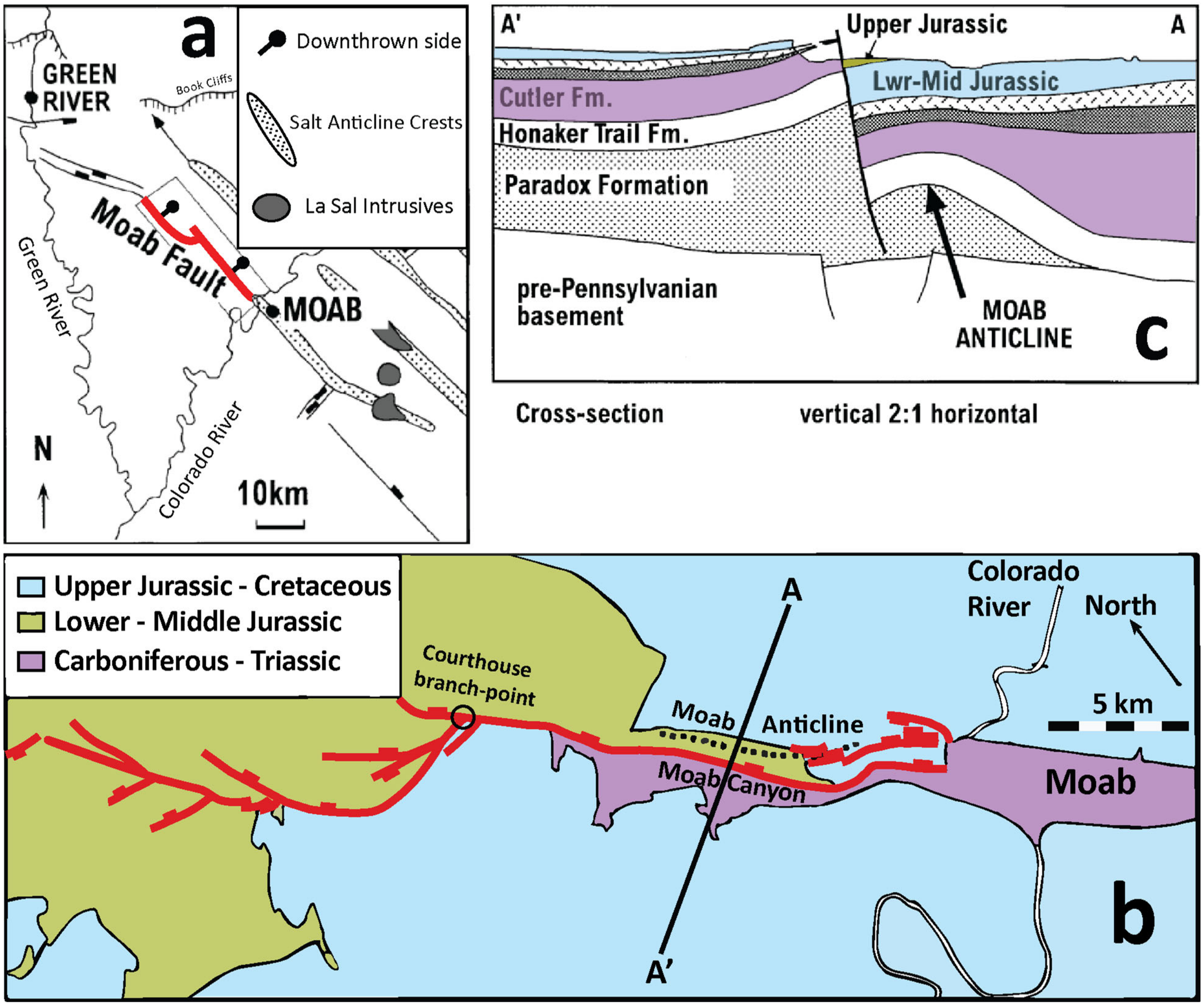


Figure 2. a) Location map of the Moab fault (red) and related salt structures. b) Map of the Moab Fault and surrounding geologic units. Fault trace is highlighted in red, with the tick marks noting the downthrown sides. c) Schematic cross-section of the Moab Fault from A-A’ (Fig. 2b.) showing vertical displacement through the point of maximum throw (Foxford et. al., 1996). Modified from Garden et. al. (2001). For details on field sites and Moab fault structure, see Figure 8.

### 2.3 Stratigraphy

The stratigraphic succession exposed in the study area includes Triassic, Jurassic, and Cretaceous age strata. The following formations are of principal interest for this study and are highlighted in light green in Figure 3.

#### 2.3.1 Permian Culter Formation

The Permian Culter Formation is not divided into members or formations along the southwestern margin of the Uncompahgre platueau where the study area of this project is located, whereas it is raised to group status elsewhere in the Paradox Basin (Condon, 1997). The Culter Formation was deposited in large part as a series of alluvial fans (Nuccio and Condon, 1996) and further distributed by rivers that crossed the coastal plains under arid conditions. The Cutler Formation is dominated by a dark red arkosic sandstone with visible mica, derived from the “Ancestral Rockies” of the Uncompaghre uplift and its thickness is up to 1,100 ft (357 m) in the Moab area (Doelling, 1987 and 1985, Doelling et. al. 2000). Salt structure forming activity started in the Pennsylvanian and increased during the Permian, causing the Culter Formation to thicken in the adjacent synclines and thin over the tops of anticlines where it was eventually eroded (Condon 1997).

#### 2.3.2 Jurassic Wingate Formation

The Jurassic Wingate sandstone is the basal part of the Lower Jurassic Glen Canyon Group, separated from the underlying Triassic Chinle Formation. This cross bedded eolian sandstone was deposited in a regional scale erg system that covered most of the Colorado Plateau (Fillmore, 2011). It's thickness ranges 250-400 ft (76-122 m) in the Moab area (Doelling, 1987 and 1985, Doelling et. al. 2000). The Jurassic Wingate Formation is a massive, well sorted, fine grained gray-pink to orange-reddish-brown weathering sandstone that forms the prominent cliffs along the Moab Valley. Exposures are decorated with streaks and stains of desert varnish (Doelling and Morgan, 2000).

### 2.3.3 Jurassic Curtis Formation – Moab Tongue Member

The Jurassic Moab Tongue Member (or Moab Member) was previously assigned as a member of the Entrada Sandstone, and is recently pending formalization as a member of the Jurassic Curtis Formation to which it correlates (Doelling & Morgan, 2000), and is classified as such in this study. The Moab Member is a pale gray to white, fine to medium grained jointed eolian sandstone that caps the underlying Jurassic Entrada Slick Rock Member, separated by the J-3 unconformity. The thickness of the Moab Tongue ranges from 60 to 100 ft (18-30m) (Doelling & Morgan, 2000). The Moab Member's light colored, massive, calcareous, cliff-forming quartzose sandstone is distinguishable from overlying and underlying strata by its horizontal and low-angle cross stratification (Doelling, 2000). The depositional environment of the Moab Member is characteristic of a sprawling dune field that evolved along the southeast margin of a shallow seaway (Fillmore, 2011). Similarities between the Jurassic Navajo Formation and the Moab Member imply that both formations were subject to bleaching due to enhanced permeability from jointing (Chan et. al., 2000, Antonelli and Aydin, 1995).

### 2.3.4 Jurassic Morrison Formation- Salt Wash Member

The Salt Wash Member of the Upper Jurassic Morrison Formation overlies the Jurassic Morrison Tidwell Member. It is a gray to yellowish-gray fluvial sandstone interbedded with horizontally discontinuous easily eroded red, gray, green-gray, maroon, and lavender slopes of mudstones. The well indurated quartzose sandstone lenses are cross bedded, fine to coarse grained, moderate to poorly sorted and weather to various shades of brown, with thicknesses that are commonly 2 to 4 ft, but can range up to 20 ft. The thickness of the Salt Wash Member is 140 to 250 feet thick (43-76m) in the study area (Doelling & Morgan, 2000). Copper deposits in the sandstone of the Salt Wash Member occur coating fractures or as disseminated splotches in the form of malachite and azurite (Doelling & Morgan, 2000; Gard, 1976). The sandstones of the Salt Wash Member were deposited by river channels, and the mudstone intervals were deposited in floodplains and lacustrine environments.

### 2.3.5 Jurassic Morrison Formation- Brushy Basin Member

The Upper Jurassic Brushy Basin Member is characteristically similar to the underlying Salt Wash member. The Brushy Basin Member is a variegated silty and clayey mudstone-dominated sequence interbedded with sandstone lenses. The sandstone lenses in the Brushy Basin member are more lithic, poorly sorted, and conglomeratic than in the Salt Wash Member. The steep, easily eroded slopes of the mudstone beds are lighter, brighter colors of maroon, green, purple, gray, and lavender than the Salt Wash Member. The mudstone beds of the Brushy Basin have a high bentonite content that have a “popcorn” texture on weathered surfaces and are understood to be derived from decomposed volcanic ashes and tuff deposits from Sierra Nevada arc eruptions (Doelling 1988; Doelling & Morgan, 2000; Turner and Fishman 1991). The depositional environment of the Brushy Basin Member is a combination of interfluvial, floodplain, laucustrine, and marginal lacustrine environments (Doelling, 1988; Turner & Fishman, 1991)). Thickness of the Brushy Basin Member in the study area ranges 350 to 400 feet (107-122 m) (Doelling & Morgan, 2000).

### 2.3.6 Cretaceous Cedar Mountain Formation

The Lower Cretaceous Cedar Mountain Formation lies unconformably on the Jurassic Morrison Formation Brushy Basin Member of the Morrison Formation. Where exposed, the Cedar Mountain Formation is characterized as a largely dull green silty mudstone with a distinctive basal light to dark brown, resistant, conglomeratic sandstone which forms a recognizable cap on the steep slopes of Brushy Basin Member mudstones (Doelling & Morgan, 2000). Less common intermediary beds of sandstone occur interbedded with the silty mudstone. Infrequent localized beds of limestone with chert nodules occur in the upper parts of the formation. Thickness ranges from 120-200 feet (37-61m). Cedar Mountain strata depositional environments are nonmarine, mainly fluvial and floodplain (Nuccio and Condon, 2000).

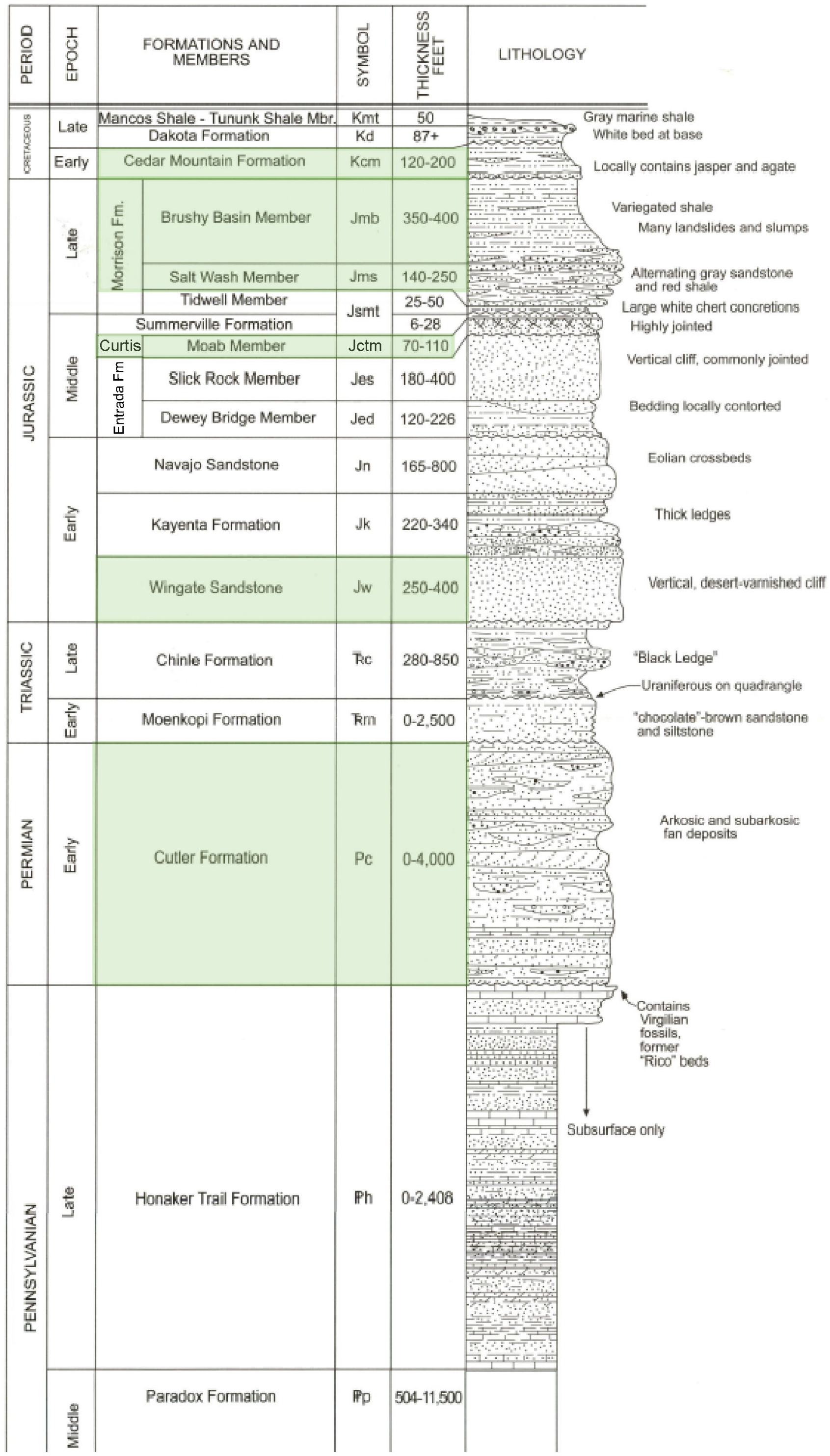


Figure 3**.** Stratigraphic section of study area. Highlighted units are outcrops encountered at study sites. Modified from Doelling, 2000.

## 2.4 Paleofluid Background

Multiple episodes of fluid flow coincide with the multiple episodes of displacement on the Moab Fault (Bergman et al., 2013; M. A. Chan et al., 2000; Chan et al., 2001; Davatzes & Aydin, 2005; Eichhubl et al., 2009; Foxford et al., 1996, 1998; Garden et al., 2001; Johansen et al., 2005; Johansen & Fossen, 2008; Solum et al., 2005, 2010). Evidence of paleofluid flow within and around the fault system has been well documented by previous studies and is readily observed in the field.

Previous workers have established multiple episodes of fluid flow involving isotopically distinct fluids during and potentially postdating documented activity on the Moab fault and general vicinity. These fluids have been demonstrated to be both deep-sourced and of shallow meteoric origin. Interactions between the deep and meteoric fluids have resulted in a complex history of element mobilization and mineral precipitation, with attendant uncertainties in chronology. In generalized form, deep basin Paradox Formation sourced brines have acted as an elemental mobilizer due to their reduced oxidation state, while shallow, meteorically-derived groundwaters have acted as a catalyst for precipitation and mineral formation, when and where the two fluids mix (Chan. et. al., 2000; Garden et. al., 2001; Eichbul et. al., 2009). Evidence of the complex paleofluid flow history and fluid mixing interaction events primarily includes: calcite cementation, bleaching of hematite-bearing strata, liesegang banding, and the presence of manganese, and minor local malachite and azurite mineralization. Uncertainty exists about the timing of flow of a given distinct fluid or interaction between deep and shallow fluids as evidenced by published age estimates of fluid flow and mineral dissolution and precipitation events overlapping, suggesting a complex spatiotemporal relationship across the greater region. A meteoric $\delta^{18}O$ isotopic fingerprint in some gouge minerals suggests that the fault system was penetrated by meteoric water during an active phase of faulting (Pevear et al., 1997). A subsequent study supports the conclusion that fluid activity along the Moab fault was involved in forming I/S (illite-smectite) in the gouge (Solum et. al., 2005).

Iron oxide reduction fronts related to bleaching in the Jurassic aeolian sandstones (Najavo and Moab Tongue Member) indicate hydrocarbon-bearing fluids flowed up the Moab fault, followed by an aqueous fluid that precipitated calcite cements (Garden et. al., 2001). Evidence also related to iron oxide reduction is indicated by leisegang banding surrounding fractures of the Moab Tongue Member and as halos in the northern splayed section of the fault (Eichhubl et al., 2009; Whitehead, 2019). Manganese oxide (MnO) mineralization occurs as black stains in fractures of Jurassic sandstones in the vicinity of the Moab fault, interpreted to have precipitated when oxygenated meteoric water encountered Paradox Formation-derived reduced saline waters in the porous sandstones (Chan et. al. 2000, 2001,). Malachite mineralization is present locally in the fault zone and is found frequently with MnO stains. In the northern structurally complex section of the Moab fault, where it splays and exhibits extensional steps at the Courthouse Rock Branch Point, malachite is abundant as fracture filling cement in joints of the bleached Moab Tongue Member and is commonly concomitant with residual hydrocarbon staining (Eichhubl et al., 2009)Regionally, malachite and azurite occur as disseminated splotches in fractures of the Salt Wash Member (Doelling, 1988; Gard, 1976).

Supergene copper mineralization in the form of malachite and azurite is historically known in the northern splayed area of the Moab fault and is evident by abandoned surface workings and prospecting pits (Foxford, 1996). Precipitation of malachite cementation in the Moab Tongue Member at the Courthouse Rock Branch area is thought to be the most recent cement phase associated with a basinal fluid source (Foxford, 1996; Eichbul, 2009). Mineralization of malachite and MnO is associated with copper bearing fluids many authors associate with Oligocene igneous activity of the La Sals (Foxford, 1996; Chan, 2001; Solum, 2010). Some mineralization of malachite may be from horizontal flow of uranium-copper fluids associated with sandstone-hosted uranium deposits of the tabular type, which are regionally well known to be present throughout the Colorado Plateau (Johnson and Thordarson, 1966).

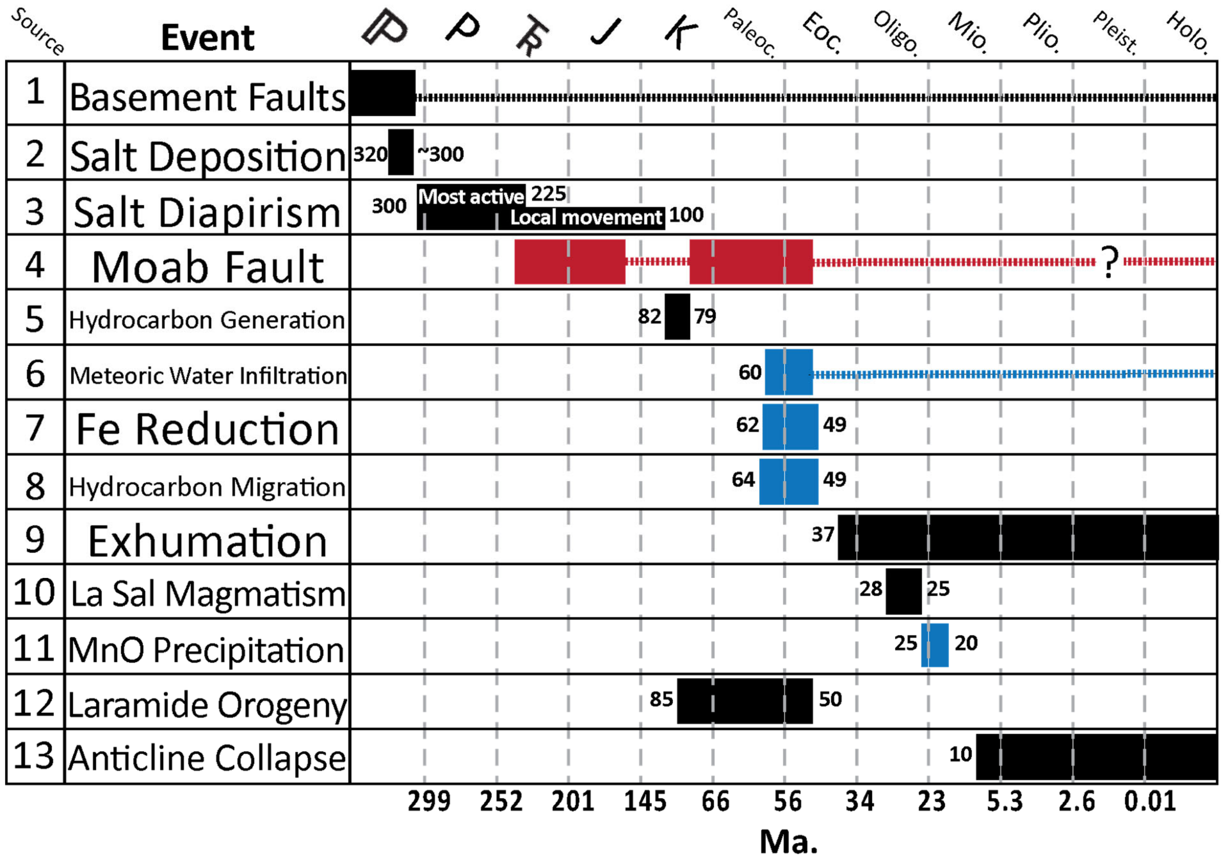


Figure 4. Diagram depicting sequence of events compiled from various sources, modified from Foxford et. al., 1996. Activity of the Moab Fault is red. Fluid flow related events are in blue. Sources cited in this figure can be found in the References section of this study: 1) and 2) Doelling, 1988; Foxford et. al., 1996. 3) and 13) Doelling ,1988. 4) Foxford et. al., 1996; Pevear, 1997; Solum et. al., 2005. 5) and 9) Nuccio and Condon, 1996. 6) Pevear 1997; Eichbul et. al., 2009. 7) and 8) Garden et. al., 2001. 10) Nelson, 1992. 11) and 12) Chan et. al. 2001.

# CHAPTER 3

# METHODS

## 3.1 Terraspec Halo Insturment

An innovation in this research is the application of very near and near infrared reflectance spectroscopy via the TerraSpec Halo Mineral Identifier (Halo), a product of Malvern Panalytical. The Halo instrument is a portable mineral identifier able to rapidly identify minerals in the field (Malvern Panlytical, 2018). Wavelength ranges scanned by the Halo include visible and near infrared (VNIR: 350-1000 nm) and short-wavelength infrared (SWIR: 1001-2500 nm). The output data, along with mineralogy, include reflectance spectra, which allow for calculation of diagnostic scalars including hydroxide bond peak locations (based on wavelength), Chlorite Spectral Maturity (CSM) and Illite Spectral Maturity (ISM) based on absorbance peak ratios. Sample collection using the TerraSpec Halo is done by powering on the instrument with its provided reference disk, removing the reference disk from the window, placing the instrument directly on the outcrop surface, and activating the trigger, keeping the instrument on the sampled surface until it chimes (about 60 seconds in duration). The instrument reports scalar measurements such as ISM values (discussed in next section) and detected minerals. Minerals are identified by matching to a “known spectrum” loaded into the Halo’s internal mineral database (Library Version 2.3 from Malvern Panalytical 2017).


Figure 5. Terraspec Halo Instrument. Top right from product field manual, left shows diameter of window. Bottom two images show the Halo in action

### 3.2 Illite Spectral Maturity (ISM)

Spectral maturity ratios are extremely useful indicators to analyze anchizonal-epizonal metamorphism (Doublier et al., 2010). As reported by the Halo, the ISM scalar indicates the grade of metamorphic maturity as a proxy for the temperature of the alteration events (a measure of illite crystallinity vs. hydration; Doublier & Roche, 2010). An ISM value of less than one indicates lower temperature alteration events, and higher ISM values indicate increasing temperature of alteration. We assume that in fault gouge, this value is affected by the temperature of the fluid passing through the gouge, particularly if gouge ISM differs notably from wall rock ISM. The value of this scalar is defined as “the ratio of the reflectance value of the hull normalized spectrum in the Al-OH absorption feature divided by the reflectance value of the hull normalized spectrum in the water absorption feature” (Malvern Panalytical, 2018).

The ISM scalar is calculated in the Halo using the reflectance spectrum of the phyllosilicates in the smectite-illite-muscovite group, which indicate a loss of molecular water. It is only reported when a mineral in this group is detected. The water ($H_2O$) absorption feature is found near 1950 nm while the aluminum hydroxide ($Al(OH)_3$) absorption feature is found near 2200 nm (Fig. 6). This study revealed ISM values ranging from near zero to above 2.

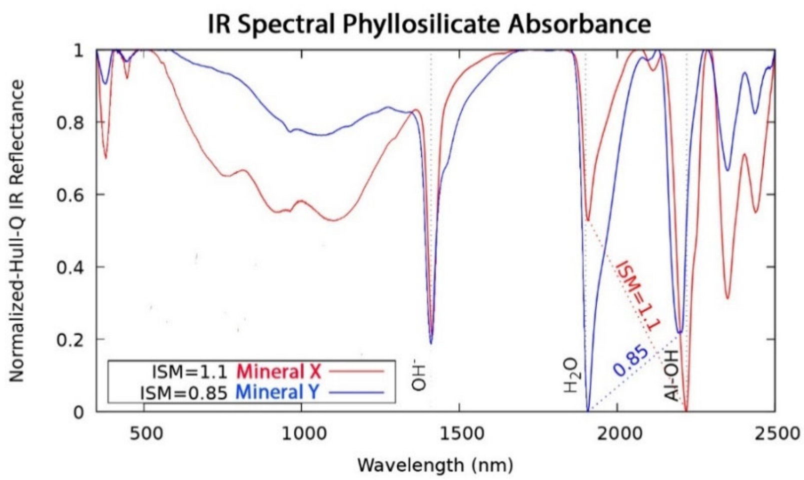


Figure 6. Infrared Spectral Phyllosilicate Absorbance. Infrared Spectral signatures measured by the Halo are scalars based on ratios of reflectance at diagnostic wavelengths. “Maturity” is interpreted as a ratio of these two absorbance peaks.

### 3.3 X-Ray Diffraction

X-Ray Diffraction (XRD) is known to be challenging and time-consuming in analyzing phyllosilicates, especially mixed-layer clay minerals. XRD confirmation of the SWIR mineral identifications reported by the Halo is beyond the scope of the present study and may be a focus of future studies. In any event, SWIR may be a more appropriate tool for regional study of fault gouge mineralogy.

### 3.4 Field Methods

To detect fault-related change in mineralogy, this study applied detailed cross-sectional scans at classic outcrop sites along the Moab Fault. The exposed outcrops were selected from previous field studies' schematic transects by Foxford et al. (1996), and significant fault exposure sites from Davatzes & Aydin (2005), and Solum et al. (2005 and 2010). In this study, three main profile sites were selected for detailed examination (Fig. 3): R191 Bike Path, Cotter Mine, and Prospect Pit. These sites introduce different problems that are useful for the evaluation of the Halo. At each site, horizontal profiles, (perpendicular to fault plane) were scanned with the Halo to include footwall, gouge, and hanging wall of each contact. Scan locations along the outcrop profiles varied from 0.1m to 5m horizontally and vertically from the horizontally placed guide tape reference. This method allows for a comprehensive data collection at and around the fault contact zone. Gouge thickness varied by site, from centimeters to several meters.

Figure 7. Example of a small-scale horizontal profile

# CHAPTER 4

# RESULTS

Three sites were selected to represent the range of Moab Fault regimes in the study area: R191 Bike Path, Cotter Mine, and Prospect Pit (Fig. 8). These profile sites were also prominent in previous studies and were selected from a total of 17 profile sites scanned in this study. The essential geologic differences between the selected sites along the length of the Moab Fault are magnitude of displacement (or throw) and lithologic juxtaposition. In the following sections, 3D Photogrammetry is used to show the large outcrop at the R191 Bike Path site, while 2D photos illustrate the remaining two outcrops. Superimposed on those photos are scan ribbons with color indicating ISM values detected along the scan points along the outcrop (Figures 9 through 11).

## 4.1 Criteria of Mineral Classification from the Terraspec Halo

In the following sections, each outcrop is sectioned into zones based on criteria pertinent to the individual outcrops, clarified in the figure captions for each profile site. Identified minerals reported by the Halo are accompanied by a “star rating” of 1, 2, or 3, based on prediction confidence where 1-star rating is least confident to 3-star rating is most confident (Malvern Panalytical, 2018). Specific minerals with a 2-star and 3-star rating were grouped into the following more general classifications: Carbonates, Kaolinites, Smectites, Illites, Micas, Epidotes, Iron Oxides, and Evaporites. Minerals and their mineral group classifications are found in Table 1 of the Appendix. Individual minerals found in each group for each profile site are listed in Tables 3, 5 and 7 of the Appendix. Pie charts in displayed in Figures 9b, 10b, and 11b represent "ISM-related" mineral assemblages reported by the Halo instrument and frequency of occurrences as percentages for each zone. "ISM-related" minerals are defined as Smectites, Illites, and Micas in this study, all having prominent Al-OH and (bound) H-OH infrared absorbance peaks, and listed in order of increasing crystallinity ("maturity", and likely formation temperature). The sum of ISM minerals detected is given ("n"), varying in each zone due to sampling frequency and IR reflection strength. Full mineral assemblages reported by the Halo can be found in Tables 2, 4, and 6 of Appendix.

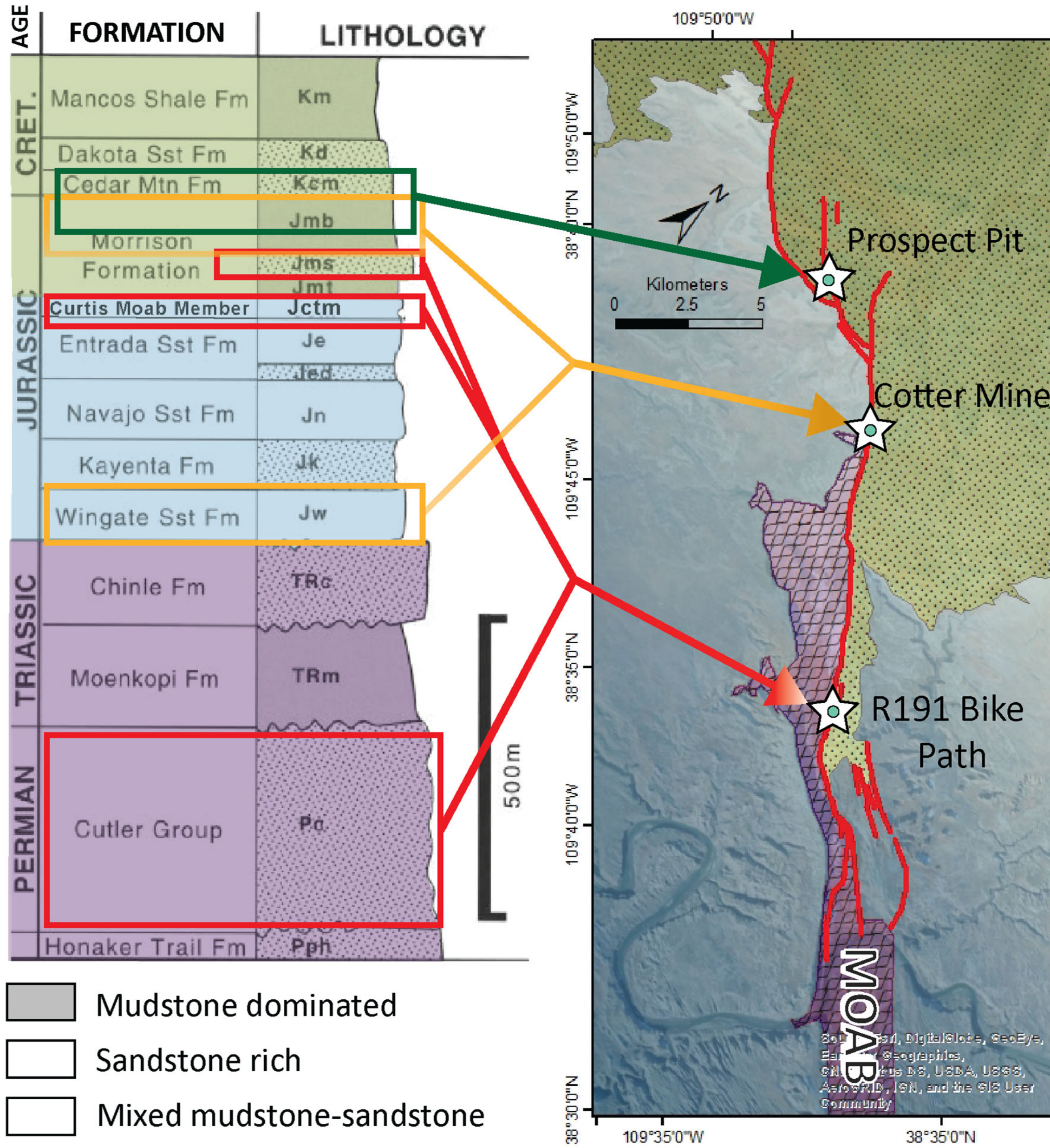


Figure 8. Map of profile sites (stars) along the Moab Fault (red) showing juxtapositions from faulting at each site (colored boxes, left). From south to north are: R191 Bike Path, Cotter Mine, and Prospect Pit. The exposed geologic units across the profile sites are correlated to the stratigraphic column (left), modified from Foxford et. al. (1996, 1998). Translucent colors superimposed on the stratigraphic column (left) and satellite image (right) are from Figure 2. The fault throw magnitude declines steadily northward.

## 4.2 R191 Bike Path (Figure 9)

At this location there are two gouge zones: the main fault plane (right) showing muted indications of alteration and the other from a vertical fault splay that shows relatively sharp changes in ISM indicators (left). The main displacement juxtaposes the Jurassic Moab Tongue Member of the Curtis Formation (Jcmt) against the Permian Cutler Formation (Pc) with an offset of ~960 meters (Foxford, 1996). The minor gouge zone (left) is between the Salt Wash Member of the Jurassic Morrison Formation (Jms) downthrown block and the Jurassic Curtis Formation; the offset of this minor vertical splay is ~60 meters (Foxford, 1996). The gouge zone is wider on the higher displacement fault than at the minor splay. There was no malachite mineralization observed in the area.

### 4.2.1 Distribution of ISM (Figure 9a)

High ISM values are detected in the sandstones of the wall rock formations and in the wide gouge zone associated with higher fault offset. These are likely inherited from the source material of the sandstones. The area with lower ISM values is within the gouge zone of the minor vertical splay, potentially reflecting post-displacement alteration. Two "moderate" ISM values of 0.765 and 0.823 were reported directly from a clay smear on the plane of the main fault.

### 4.2.1 Distribution of Minerals (Figure 9b)

Elevated smectite/illite can be interpreted to indicate reduced mineralogical maturity, and therefore lower mineral formation or alteration temperature. In Zones 1 through 3, the average smectite to illite ratio is 0.98 (light vs. dark green, Fig. 9b), indicating about an equal number of detections of smectite versus illite in the low throw gouge zone; however, in Zone 4, the detections of smectite significantly decrease in the sandy Moab Tongue Formation and is not detected in Zones 5 and 7. The detections of micas in Zones 1 and 2 (orange, Fig. 9b) are approximately equal to the detections of smectite but is significantly lower in Zone 3. In Zone 4 (Moab Tongue Formation) and 5 (the large gouge zone), micas make up two thirds of the amount of ISM-related minerals, and half of the ISM-related minerals detected in Zone 7 located in the Cutler Formation. In Zone 6, illites are the majority of ISM-related minerals with a 3 star rating, and a 2-star rated smectite, specifically Iron Saponite (Table 3, Appendix) were detected from the clay smear located directly in the main fault plane. Additional minerals worth mentioning in Zones 5 and 7 are iron oxides, specifically hematite (Table 2, Appendix). In summary, high-maturity mica tends to dominate the ISM-related mineralogy of the wall rocks, while low-maturity smectite becomes important in the leftmost gouge zone.

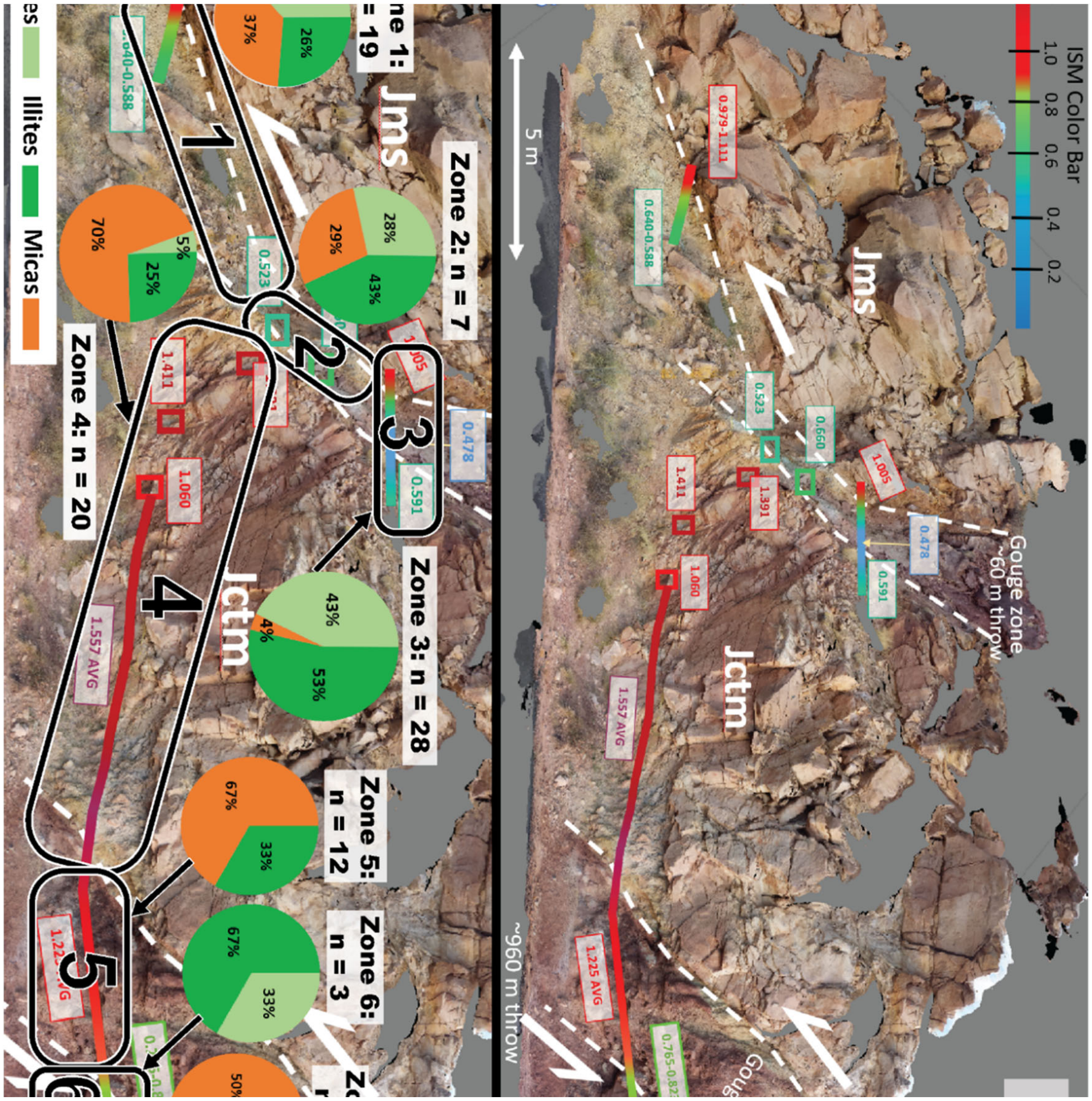


Figure 9. a) R191 Bike Path Site. 3D Photogrammetry was used to construct image to display entire rock face. Dashed white lines represent contacts of fault gouge zones. Boxed colored numbers indicate ISM values and color corresponds to ISM value on color bar (top left). Sampling frequency is approximately every 10 cm. b). Magnified section of 9a. Zones are classified by similar ISM ranges and fault zone components (i.e., gouge zones and wall rock). Relative abundances of ISM-related minerals for each zone shown by pie charts, total number of ISM-related mineral detections in each zone given by “"n”.

### 4.3 Cotter Mine (Figure 10)

Although displacement of the Moab Fault is smaller at this site, indications of fluid flow are more prominent as indicated by lower ISMs in the gouge zone and evidence of aqueous mineralization. Located approximately 8.6 km NW of the R191 Bike Path site (Fig. 8) is the Cotter Mine profile site (Fig. 10). The main fault is clearly exposed in excavations at the Cotter Mine outcrop, where the footwall Jurassic Wingate Formation is juxtaposed against the hanging wall Morrison Formation with an estimated throw of ~585 m (Foxford, 1996). The main gouge zone is within a few meters of the exposed fault plane on the Jurassic Wingate Formation (left side, Fig. 10a), grading into a damage zone in the Jurassic Morrison (center). Authigenic malachite is present, concentrated along fractures in nodular sandstone bodies of the Morrison Formation within the damage zone (Zone 5, Fig. 10a), strongly indicative of post-displacement mineralizing fluids.

#### 4.3.1 ISM Spatial Distribution (Figure 10a)

There is a familiar variation in ISM value distributions: mature ISMs in the Wingate sandstone and fault plane and immature ISMs in the identified gouge zone. A complexity here is that ISM values remain low in the Jmb toward the right, away from the fault (Fig. 10a), suggesting low original formation temperature or thorough post-deposition low temperature alteration. The damage zone appears to reflect some low temperature alteration, since average ISM within the damage zone is 0.514, whereas the average ISM of wall rocks is 1.6. An abnormally high ISM measurement of 2.843 (presumably inherited from the protolith) from a clast of sandstone containing malachite in Zone 5 (Fig. 10b) was not included in the damage zone average. A possible hypothesis to investigate here is the possibility of clay mixing from the Morrison Formation via fault smear in the gouge zone.

#### 4.3.2 Distribution of Minerals (Figure 10b)

In Zone 1, only illites and micas were detected by the Halo. In Zones 2 and 3, while smectites make up the majority of ISM minerals detected, the smectite/illite ratio decreases to the right from gouge through damage zone into the structurally undisturbed formation (Jmb) with an exception in Zone 6. Iron oxides were identified by the Halo only in Zones 1 through 3 (Table 4, Appendix), consistent with the strong reddish appearance of the gouge. In Zone 5, the Halo identified malachite (associated with a 2.843 ISM value) as well as carbonates, specifically calcite (Table 5, Appendix) which may be associated with fracture filling cements in the host rock, consistent with findings in other studies (Foxford et. al., 1996; Garden et. al., 2001; Eichbul et. al., 2009.). Although the ratio of illite to smectite in Zone 6 is 0.86, epidotes were detected (Table 4, Appendix), potentially indicating post-depositional alteration.

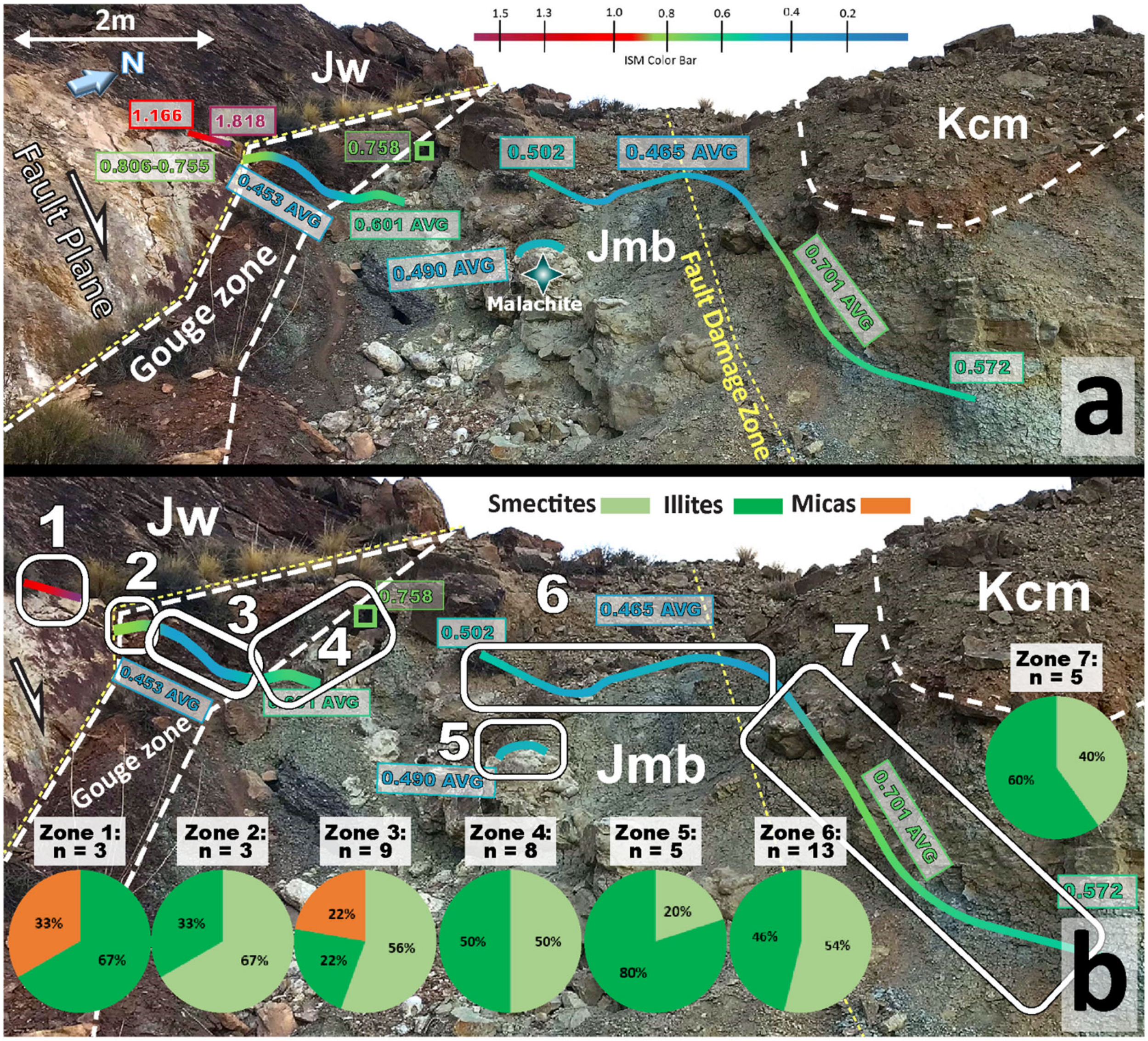


Figure 10. a). Image of Cotter Mine outcrop site. Colors indicate ISM value ranges correlating to ISM color bar. Green star indicates presence of malachite. The fault plane is exposed at surface (left). Jw is Jurassic Wingate Formation and Jmb is Jurassic Morrison Formation and Kcm is Cretaceous Cedar Mountain Formation. b). Magnified section of 10a. Zones are classified by similar ISM ranges and fault zone components (i.e. hanging wall, gouge zone, damage zone, footwall).

### 4.4 Prospect Pit (Figure 11)

The northernmost profile site Prospect Pit is located approximately 4.3 km NW of Cotter Mine, on a minor splay of the Moab Fault. The formations involved here are the hanging wall Jurassic Morrison Formation Brushy Basin Member and the footwall Cretaceous Cedar Mountain Formation, where the offset could be less than 100m (Foxford, 1996). At this site, it was more difficult to structurally and texturally discern fault gouge. There is an abundance of malachite and manganese oxide staining in the sandstone beds of the Brushy Basin Member, strongly indicating presence of mineralizing fluids.

#### 4.4.1 Distribution of ISMs (Figure 11a)

There is a familiar distribution again, where higher ISM values were reported mostly in the sandstone beds and lower ISMs in the greener clay beds (Fig. 11a). Since gouge was difficult to identify at this site, ISM trends relative to the fault plane are obscure, and tend to follow bedrock lithology instead (see Chapter 5: Discussion).

#### 4.4.2 Distribution of Minerals (Figure 11b)

Throughout Zones 2 through 5 indicated in Fig. 11b, illite makes up half to two thirds of the ISM-related minerals detected, except in Zone 1 where illite was the only ISM-related mineral detected. Significant amounts of mica were detected in Zones 2 and 3, primarily in sandstone blocks, and consequently exhibiting higher ISM values.

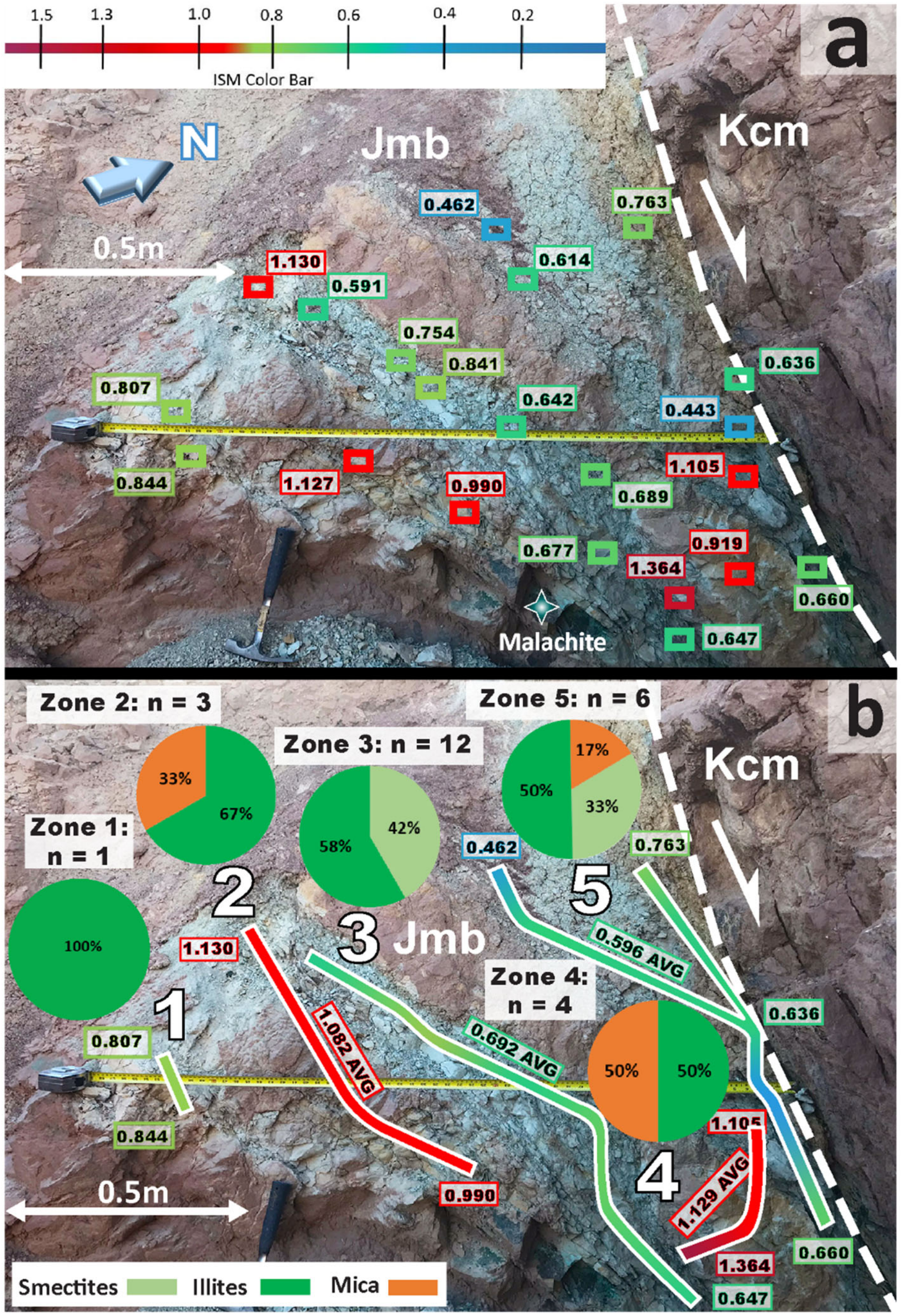


Figure 11. Image of Prospect Pit site. a). Boxes indicate sample scan point locations and colors correlate to ISM color bar (top left). Green star indicates presence of malachite and Mn-oxides on small fractures in sandstone. The fault plane is exposed on the right between the Brushy Basin Member of the Jurassic Morrison Formation (Jmb) and the Cretaceous Cedar Mountain Formation (Kcm). b). Same outcrop image as 11a. Zones are represented by colored ribbons correlating with the ISM color bar in 10a. Zones are classified by similar ISM ranges and lithology.

# CHAPTER 5

# DISCUSSION

The goal of this project was to assess the effects of fluid migration in fault zones cutting sedimentary sequences using field collected IR spectroscopic analysis of gouge minerals. In the specific setting of the Moab Fault, the project sought the relative contributions to the gouge by fault smear of sedimentary clays vs. post-displacement authigenic mineral growth. Field IR spectroscopy has been highly successful in assessing hydrothermal alteration in igneous porphyries (high temperature, e.g., Dalm, et al. 2014), moderately successful in paleo-geothermal systems (low-grade metamorphic, Chinomso & Brikowski, 2016), and in this project with mixed success in evaluating very low temperature alteration. That variable success reveals important aspects of the fluid alteration history in the vicinity of the fault, and the strengths and weaknesses of the field IR approach in addressing such issues in sedimentary settings.

The portable Terraspec Halo specifically identifies hydrated silicates quite well, and reports diagnostic spectral scalars (e.g., ISM) that help constrain likely mineral formation/alteration conditions., This data allows us to make inferences about paleo fluid flow, types of fluids, temperature of alteration, distinguish inherited from altered/neoformed clays, and the effects of fault displacement on pervasiveness of flow and degree of alteration, all without the more traditional use of labor-intensive XRD techniques. The sites selected for sampling show systematic variations in paleo fluid flow regimes and alteration degree and products, with implications for structural and lithologic controls on fluid flow.

## 5.1 Interpreting Clay Mineral Alteration in Gouge with ISM

The geologic setting for this study is primarily sedimentary, with alteration typical of diagenetic-zeolite-anchizonal “metamorphism” and/or low-temperature metasomatism. ISM scalars (ratios of IR absorbence peaks) give an indication of the ratio of sheet silicates’ mineralogic maturities vs. degree of hydration (Fig. 6). Spatial variation in ISM relative to the fault can indicate fault-related fluid migration and rock alteration. In general, high maturity (more crystalline, less hydrated) requires higher formation or alteration temperatures than low maturity (Doublier & Roache, 2010). Then with increasing temperature (metamorphic grade) a transformation from smectite to a mica (muscovite) is expected, specifically smectite → mixed illite/smectite (I/S) → illite → muscovite (mica). Lower ISMs indicate a less mature, less crystalline, and more hydrated minerals whereas higher ISMs indicate mature, more crystalline, and more dehydrated minerals. ISMs from sand or siltstones are generally high since their hydrated silicate grains are matured and highly crystalline (e.g., micas inherited from a metamorphic or igneous sedimentary source).

The long geologic history of the Moab fault suggests several superimposed sequences of gouge formation and alteration could be present (Fig. 12). Initially (Stage I) clay minerals that developed from mechanically derived clay smears during faulting would give a "neutral” ISM value ($\approx 1, \pm 0.2$). Next in Stage 2, as hotter fluid flow upward through the fault zone (brines formed during dissolution of the deeper salt tectonism), clay minerals within the clay smears of the fault gouge would be altered producing a higher maturity and therefore a high ISM reading

(~ >1.2) and could be accompanied by hotter temperature mineralization (e.g., sulfides that might ultimately weather to malachite). Higher ISMs may also be interpreted as deriving from inherited wall rock grains in the gouge zone, given that the wall rock contains mature, often mica-bearing sandstone. In Stage 3, alteration and authigenic formation of clay minerals within the fault zone from cool meteoric fluids overprint the previous signatures from Stage 2 and will yield lower ISM readings (~< 0.8) along with increased development of smectites and zeolites. A possible limitation of this approach is if there was only a Stage II that followed Stage I or only a Stage III that followed stage 1.

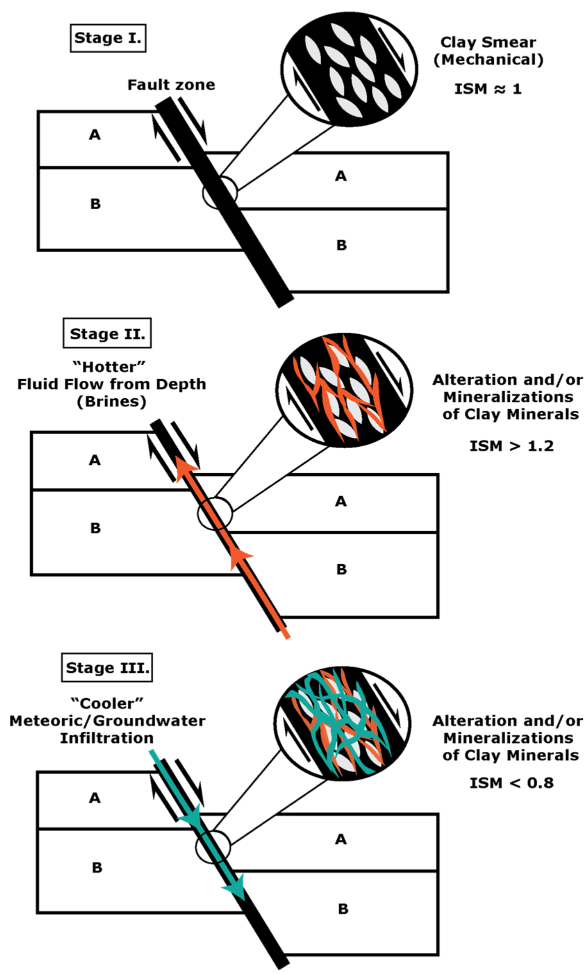


Figure 12. Schematic diagram of expected concepts applied to the Moab Fault

## 5.2 Scalar and Mineralogical Indicators of Fluid Effects

In the design of the project, scalars (absorbance peak ratios, Section 3.2) were expected to be the primary line of evidence for fluid effects in the fault zone. In gouge, such effects were interpreted to be visible in the low-throw fault zone at R191 Bike Path (left side, Fig. 9a). Distinctly low ISM (< 0.5) spatially high in that zone is a strong indication of late, low temperature alteration. A puzzle is that the ISM signal of alteration appears weaker on the major-throw fault zone at R191 (right, Fig. 9a), although the difference between minimum and average ISM in that zone is large. Since the Halo averages signal over a 1 cm radius, it may be that the minimum ISM in the major-throw gouge (0.765) is an amalgamation of lower ISM minerals with inherited grains from the wall rock, with ISM >= 1.2.

ISM results were broadly consistent across sites, recording high ISM values in sandstone dominated wall rock and the hematitic dominated gouge (Fig. 9 and Fig. 10). However, sedimentary lithology seems to exert a control on this relationship as seen in Figure 11 and the right side of Figure 10. Wall rock lithology with high clay content (i.e., Jurassic Morrison Brushy Basin Member) exhibit a gentler, although slightly distinguishable, contrast in ISM values.

We identified low temperature fluid alteration at all three sites, the clearest "endmember" at the R191 Bike Path (left side, Fig. 9), fairly clear at Cotter Mine (Fig. 10) and the complicated endmember Prospect Pit (Fig. 11). Low ISM readings recorded in fault gouge zones of the R191 Bike Path and Cotter Mine sites show expected trends in the damage zones where they may have been altered by fluids. In Zone 3 (gouge zone of the lower throw fault splay) of R191 Bike Path (Fig. 9b), the abundant smectite detected paired with low ISMs is consistent with low temperature alteration (Section 5.1). However, in most of the large gouge zone associated with the highest throw fault of R191 Bike path (Zones 5 and 6, Fig. 9b), the ISM values remain elevated, and the majority of minerals detected are interpreted to be inherited micas from the Cutler Formation (orange part of Zone 5). This result is unexpected (Fig. 12) and suggests that little to no alteration that occurred and the slightly lower ISM values in the clays smear of Zone 6 could be of mechanical origin. This study is designed to assess post-faulting fluid alteration and neoformation of clay minerals, and analysis of mechanically- formed clay smears is outside of the scope of this project. Regarding the abundance of smectites in the gouge Zones 1 through 3 of R191 Bike Path relative to the wall rock (Fig. 9b), this leads us to believe that the smectites are enhanced by fluids and therefore altered. Our results suggest minimal fluid migration along the Moab Fault at the R191 Bike Path site in the large-throw gouge zone (right side, Fig. 9). These results differ from the conclusion from previous studies employing different methodology, which involved microscopic techniques and analysis of illite-smectite polytypes (Solum et. al. 2005, Solum et. al. 2010) suggesting that there was “major fluid involvement” at this site. In contrast, the measurements in this study are of a more “macro” scale and presents a different interpretation than Solum et. al. (2005), perhaps masking a major process.  At the Cotter Mine site there was stronger evidence of fluid flow within the gouge zone. The presence of decreased ISM values and elevated abundance of smectites in the gouge zone (Zones 2 and 3, Fig. 10b) suggest involvement of fluid alteration indicative of Stage III type alteration (Fig. 12).

### 5.3 Areas of Model Success

IR spectral analysis and ISM function best when combined with discrete counts of ISM-related minerals (Smectite, Illite, Muscovite). In this study we observe that both ISM and abundances of smectite, illite, and muscovite vary systematically within and outside of gouge zones, controlled by paleo fluid interactions and lithology. Within and adjacent to gouge zones, we find that ISMs generally decrease, the abundance of smectite and illite increase, and muscovite decreases relative to country or wall rock. Abundance of smectite and low ISM is thus a strong indicator of fluid interaction. These relationships are best shown in the R191 Bike Path and Cotter Mine sites where gouge and damage zones have relatively low ISMs, high smectite ratios, and relative mica abundance serves as a proxy for matured minerals interpreted to be inherited from wall rock lithology. Notably, Zones 5 and 6 in the R191 Bike Path site do not conform to this model, as was discussed earlier. The Prospect Pit site is less clear, and this may be attributed to the low magnitude of displacement on this fault section, providing for poor gouge zone development. However, the lowest ISM values and high smectite abundance are recorded in the narrow fault gouge that is present, along the fault plane (Fig. 11, Zone 5). Variations along other zone transects likely reflect more on the varying lithologies present in the Brushy Basin member of the Morrison Formation. Results presented at the Prospect Pit gives weak evidence of along fault flow. The presence of malachite (Fig. 11a) argues for horizontal or along bed flow (e.g., Thomas, et al., 1991), and the lack of any visible alteration in the Cedar Mountain Formation may indicate the fault at this location acted as a barrier to flow.

### 5.4 Limitations on Model Success

Though demonstrated as a useful tool for rapid identification and mapping of clay minerals, possible fluid alteration zones, and first-order analysis of paleofluid events, the Terraspec Halo has apparent limitations in this application. Though there may be easily identified field evidence for fluid alteration and past flow such as mineral occurrences and textural observations, ISM data is not always suggestive of such. Malachite is easily observed at the Prospect Pit site (Fig. 11), undoubtedly from fluid alteration, however, ISM measurements made adjacent to that occurrence (Fig 11, Zone 2) record relatively high ISM values (1.082 average). Within the framework of this study, that would imply little to no fluid interaction. This could suggest that certain lithologies are poor candidates for ISM analysis, such as sandstones with low clay contents. Figure 11 exemplifies this well as the high ISMs are within sandstone lenses of Jmb (Fig. 11, Zones 2 and 4). A similar case may exist at the R191 Bike Path shown in Figure 9, the well-developed gouge zone (Fig 9, Zones 5 and 6) incorporating the Permian Cutler Formation, an immature arkosic sandstone, records almost entirely high ISMs along a transect. Traditional and more precise laboratory methods can report results contrary to the methods employed in this study, as discussed above (Section 5.2). Similarly at the well-developed gouge zone at the Cotter Mine site (Fig. 10), the gouge is heterogeneous and ISM measurements may differ depending on whether matrix or clasts of country rock entrained in the gouge zone are scanned.

Care should be taken to not mix lithologies and textures during measurement transects when avoidable. When measuring rock units which have complex internal stratigraphy, such as Jmb at the Prospect Pit study site, variations in ISMs and mineral abundances can be due to sampling different lithologies, such as the clayey layers vs the sandy or silty lenses, or rare carbonate beds. In clay dominated units, distinguishing damage zones and gouge from intact but weathered country rock can be a challenge in the field and can greatly complicate interpretation of results. Clay size fraction dominated units also will necessarily have a lower ISM, so the contrast between fluid altered gouge or damage zone and intact unaltered country rock will be muted.

IR analysis primarily reflects the most recent fluid event but may also be unable to resolve and distinguish between multiple low temperature fluid alteration episodes. In Zones 5 and 6 at the Cotter Mine site, (Fig 10b) there is evidence for a low temperature metasomatic event given by the physical presence of malachite in Zone 5, however, the decreased ISMs and higher smectite to illite ratio within the damage zone of Zone 6 suggests evidence for possible meteoric infiltration in the damage zone (Fig. 10). We were unable to distinguish these two fluid events by solely pairing ISM and ISM-related mineral detections with the Halo. To further discern that there were multiple fluid events in the damage zone of Cotter Mine (Fig. 10), we incorporate the additional non-ISM related minerals detected by the Halo in Zones 5 and 6 (Fig. 10b) into interpretations. Malachite and calcites were detected by the Halo in Zone 5, and epidotes were detected in Zone 6 (Table 5, Appendix), which may be indicative of a metasomatic event carrying copper and carbonate bearing fluids into the damage zone. We interpret the scenario of the Cotter Mine site was that a low temperature metasomatic event, responsible for mineralizing the malachite, epidote, and possibly magnesium oxides, occurred as Stage II, followed by infiltration of a cool temperature meteoric downwelling fluid as Stage III (Fig. 12) that would further lower ISM values.

In situations where field observations clearly indicate a well-developed gouge and damage zone, but IR analysis implies little or no fluid alteration, additional traditional XRD and/or SEM laboratory analysis may be warranted, as evidenced in the R191 Bike Path site (Fig. 9, Zones 5 and 6).

### 5.5 The Perplexing Presence of Malachite at Cotter Mine and Prospect Pit

The source and mechanism of emplacement of Cu-Mn mineralization present at the Cotter Mine and Prospect Pit sites are enigmatic, especially that the most abundant occurred at the Prospect Pit site where there is the least magnitude of fault displacement (< 100 m) and is interpreted as being a barrier to fluid flow. At both sites, malachite occurs within fractures of Jurassic sandstone lenses or bodies accompanied by black manganese oxide staining and mineralization.  As previously discussed in section 5.5, the mineralization of malachite in the damage zone of Cotter Mine may have been from a metasomatic event that was followed by a meteoric infiltration. On the other hand, at the Prospect Pit, there is not an easily discernable indication of meteoric infiltration, yet there was the most prominent malachite mineralization at this site, even with a minor amount of azurite.

Various concentrations of copper bearing mineralization (such as malachite and azurite) occur in fractures of sandstone units in large regions throughout the Paradox Basin and Colorado Plateau provinces and are the result of metasomatic fluid events due to mobilization of copper bearing fluids in basement rocks affected by Laramide and later tectonic events, and that these fluids may travel through the same pathways as petroleum systems (Barton et al., 2018; Chan et al., 2000; Eichhubl et al., 2009; Garden et al., 2001). Other studies of the region within the Colorado Plateau and the Paradox Basin suggest copper mineralization is related to tabular uranium deposits of the regional Jurassic sandstones, implicating a horizontal flow regime type (Johnson and Thordarson, 1966). Gard (1976) and Doelling (1988) indicate that malachite and azurite occur in the Jurassic Morrison Salt Wash Formation in the Paradox Basin, regionally close to the Moab Fault. Studies noting local malachite mineralization accompanying calcite cementation in fractures of porous Jurassic sandstones of the Moab Fault (Foxford, 1996; Eichbul, 2009) suggest that mineralization is associated with a basinal fluid source and have the pot. A recently released study suggests that there was a second phase of fluid migration in the Moab Fault in the Courthouse branch point area (Fig. 2) that remobilized copper from its original mineralization (Bailey et al., 2021). All of these studies enhance the complexity of the origin of malachite mineralization. Were there different regimes of copper bearing fluids flowing in the vicinity of the Moab Fault at different times? Perhaps the origin of malachite mineralization at Cotter Mine is different than at Prospect Pit. A possibility is that the malachite at the Prospect Pit may have been due to remobilized copper bearing fluids.

# CHAPTER 6

# CONCLUSION

This study demonstrates that IR spectral analysis can be adapted with mixed success for use in low temperature fluid alteration in sedimentary environments. The usefulness of IR spectral analysis is greatest when employed as a reconnaissance tool for large projects to identify sites where laborious, traditional, and expensive analytical methods, is warranted. In this way the Terraspec Halo can allow the researcher to minimize time and resources expended on XRD and SEM analyses when investigating low temperature alteration events in sedimentary rock settings. As is shown, the IR data combined with careful field observations yielded relatively straightforward to interpret data in some situations, while being much more ambiguous in others; it is in those ambiguous cases where samples should be taken and subjected to the aforementioned traditional analytical methods. While its use as a reconnaissance tool in this environment is promising, no paleofluid analysis should rely on these results without corroborating lines of evidence.

IR analysis did produce interpretable results which suggest both high and low temperature fluid alteration of the sedimentary rocks, especially those directly involved in the Moab fault, did occur. Some inferences can be made about the general composition of such fluids. However, absent well established literature on the subject, this study would have had to include significant XRD and SEM analysis to confirm findings and reach definitive conclusions. The inferences on the nature of these fluids and alteration products broadly agrees with the conclusions of prior work, with some exceptions outlined in the preceding discussion. Fault systems with long, complex geologic and hydrologic histories, like the Moab fault may lessen the interpretability of this method in isolation.

## APPENDIX

## SUPPLEMENTAL TABLES FOR CHAPTER 4

Table 1. Classifications of individually detected minerals by the Terraspec Halo into Mineral Groups (bolded). The difference between Kaolinite PX and WX is crystalline structure where PX is “poorly crystalline” and WX is “well crystalline.”

| **Carbonate** | **Kaolinite** | **Smectite** | **Illite** | **Mica** | **Epidote** | **Fe Oxides** | **Evaporites** |
|---|---|---|---|---|---|---|---|
| Ankerite | Kaolinite PX | Montmorillonite | I/S | Muscovite | Epidote | Hematite | Gypsum |
| Strontianite | Kaolinite WX | Beidellite | K-illite | Phengite | Clinozoisite | Goethite | Borax |
| Calcite | Halloysite | Rectorite | Mg-illite | Palygorskite | Zoisite | Ferrihydrite | |
| Dolomite | Dickite | Nontronite | Na-illite | Vermiculite | | Jarosite | |
| Cerussite | | Saponite | NH3_I/S | Lepidolite | | Clinohumite | |
| Kutnohorite | | Fe-Saponite | | Paragonite | | | |
| Witherite | | Fe-Smectite | | Biotite | | | |
| | | Aliettite | | Hydrobiotite | | | |
| | | | | | | | |

Table 2. Pie charts of full mineral group detections for R191 Bike Path.

| Zone | Minerals Detected | Smectite | Illite | Mica | FeOxide | Kaolinite | Evaporite | Carbonate | Epidote | SUM (n) |
|---|---|---|---|---|---|---|---|---|---|---|
| 1 | 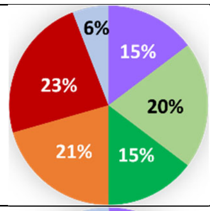  | 7 | 5 | 7 | 8 | 5 | 2 | 0 | 0 | 34 |
| 2 | 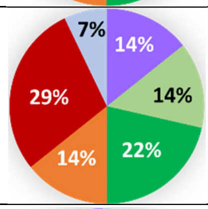  | 2 | 3 | 2 | 3 | 2 | 1 | 0 | 0 | 13 |
| 3 | 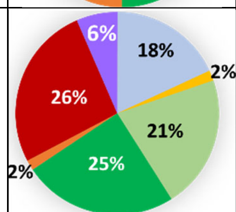  | 12 | 15 | 1 | 14 | 4 | 11 | 0 | 1 | 58 |
| 4 | 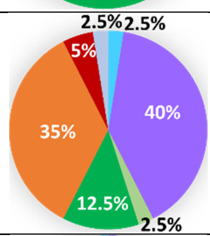  | 1 | 5 | 12 | 2 | 16 | 1 | 1 | 0 | 38 |
| 5 | 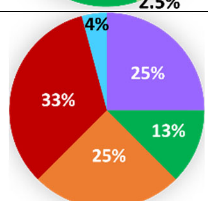  | 0 | 3 | 6 | 8 | 6 | 0 | 1 | 0 | 24 |
| 6 | 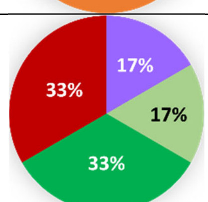  | 0 | 2 | 0 | 2 | 1 | 0 | 0 | 0 | 5 |
| 7 | 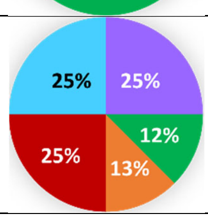  | 0 | 1 | 1 | 2 | 2 | 0 | 2 | 0 | 8 |

Table 3. Detailed mineral detections for R191 Bike Path. Minerals listed are followed by their star rating. Abbreviations of minerals are: Montmorillonite (Mont.); Beidellite (Beid.); Iron Saponite (Fe-Sapo.); Illite/Smectite (I/S); Phengite (Pheng.); Ferrihydrite (Ferrihyd.).

| Zone | # ID | ISM | AVG ISM | Smectite | | Illite | Mica | | Fe Oxide | | Kaolinite | Evaporite | Carbonate | Epidote |
|---|---|---|---|---|---|---|---|---|---|---|---|---|---|---|
| 1 | 90 | 0.979 | 0.695 | | | | Phengite, 3 | | Hematite, 3 | | Halloysite, 3 | | | |
| | 91 | 1.111 | | | | | Phengite, 2 | | Ferrihyd., 3 | | Halloysite, 3 | | | |
| | 92 | 0.711 | | Mont., 3 | | | Phengite, 3 | | Hematite, 3 | | | | | |
| | 93 | 0.64 | | Mont., 3 | | | Phengite, 3 | | | | | | | |
| | 94 | 0.588 | | Mont., 3 | | Mg-illite, 3 | | | Goethite, 3 | | | | | |
| | 95 | 0.614 | | Mont., 3 | | | Phengite, 3 | | Jarosite, 3 | | | | | |
| | 96 | 0.59 | | Mont., 3 | | | Phengite, 2 | | Ferrihyd., 3 | | | Gypsum, 3 | | |
| | 97 | | | | | I/S, 3 | | | Jarosite, 2 | | Dickite, 3 | | | |
| | 98 | 0.655 | | Mont., 3 | | | Muscovite, 3 | | | | KaolinitePX, 3 | | | |
| | 99 | 0.366 | | Mont., 3 | | Mg-illite, 2 | | | | | | Gypsum, 3 | | |
| | 100 | | | | | I/S, 3 | | | Goethite, 3 | | KaoliniteWX, 3 | | | |
| | 101 | | | | | I/S, 3 | | | | | | | | |
| 2 | 102 | 0.523 | 0.871 | Mont., 3 | | Mg-illite, 3 | | | Jarosite, 3 | | | | | |
| | 103 | | | | | I/S, 3 | | | Goethite, 3 | | | | | |
| | 104 | 0.873 | | | | Mg-illite, 2 | | | | | Halloysite, 3 | | | |
| | 105 | 0.66 | | Mont., 3 | | | Phengite, 3 | | Goethite, 3 | Jarosite, 2 | | Gypsum, 2 | | |
| | 106 | 1.428 | | | | | Muscovite, 3 | | | | Halloysite, 3 | | | |
| 3 | 137 | | 0.589 | | | | | | | | | | | |
| | 138 | 1.005 | | | | Mg-illite, 3 | | | | | Halloysite, 3 | | | |
| | 139 | | | Mont., 3 | | | | | | | KaolinitePX, 3 | | | |
| | 140 | | | | | I/S, 3 | | | Goethite, 3 | | KaoliniteWX, 2 | | | |
| | 141 | 0.411 | | Mont., 3 | | | | | Goethite, 3 | | | Gypsum, 3 | | |
| | 142 | | | | | I/S, 3 | | | Goethite, 3 | | | Gypsum, 3 | | |
| | 143 | 1.103 | | | | | Phengite, 2 | | | | Halloysite, 3 | | | Epidote, 3 |
| | 144 | | | | | I/S, 3 | | | Goethite, 3 | | | Gypsum, 3 | | |
| | 145 | | | Beid., 3 | | | | | Ferrihyd., 3 | | | Gypsum, 2 | | |
| | 146 | | | | | I/S, 3 | | | Goethite, 3 | | | Gypsum, 3 | | |
| | 147 | 0.474 | | Mont., 3 | | | | | Jarosite, 3 | | | Gypsum, 3 | | |
| | 148 | 0.523 | | Mont., 3 | | Mg-illite, 3 | | | | | | Gypsum, 2 | | |
| | 149 | 0.463 | | Mont., 3 | | Mg-illite, 2 | | | | | | Gypsum, 3 | | |
| | 150 | 0.453 | | Mont., 3 | | Mg-illite, 3 | | | | | | Gypsum, 2 | | |
| | 151 | | | | | I/S, 3 | | | | | | | | |
| | 152 | 0.276 | | Mont., 3 | | Mg-illite, 2 | | | Hematite, 3 | | | Gypsum, 3 | | |
| | 153 | | | | | I/S, 3 | | | | | | Gypsum, 3 | | |
| | 154 | | | | | I/S, 3 | | | Goethite, 3 | | | | | |
| | 155 | 0.557 | 0.589 | Mont., 3 | | K-illite, 3 | | | Goethite, 3 | | | | | |
| | 156 | 0.624 | | Mont., 3 | | K-illite, 3 | | | Goethite, 3 | | | | | |
| | 157 | | | Mont., 3 | Rectorite, 3 | | | | | | | | | |
| | 158 | | | | | I/S, 3 | | | Ferrihyd., 3 | | | | | |
| | 159 | | | Mont., 3 | | | | | Ferrihyd., 3 | Goethite, 2 | | | | |
| | 160 | | | | | | | | Goethite, 3 | Jarosite, 3 | | | | |

Table 3 Continued

| Zone | # ID | ISM | AVG ISM | Smectite | | Illite | Mica | | Fe Oxide | | Kaolinite | Evaporite | Carbonate | Epidote |
|---|---|---|---|---|---|---|---|---|---|---|---|---|---|---|
| | 107 | 1.391 | | | | | Muscovite, 3 | | Goethite, 3 | | Halloysite, 3 | | | |
| | 108 | 1.411 | | | | | Muscovite, 3 | Phengite, 2 | | | Halloysite, 3 | | | |
| | 109 | 0.765 | | | | | | | | | KaolinitePX, 3 | Gypsum, 2 | | |
| | 110 | 1.06 | | | | | Phengite, 3 | | | | Halloysite, 3 | | | |
| | 111 | 1.677 | | | | Mg-illite, 3 | | | | | KaoliniteWX, 3 | | | |
| | 112 | 1.543 | | | | | Muscovite, 3 | | | | Halloysite, 3 | | | |
| | 113 | 1.426 | | | | | Muscovite, 3 | Phengite, 2 | | | Halloysite, 3 | | | |
| 4 | 114 | 1.719 | 1.338 | | | | Muscovite, 3 | | | | KaoliniteWX, 3 | | | |
| | 115 | 1.104 | | | | | Muscovite, 2 | | | | Halloysite, 3 | | | |
| | 116 | 2.036 | | Mont., 3 | | | Muscovite, 2 | | | | KaolinitePX, 3 | | | |
| | 117 | 1.34 | | | | | Phengite, 3 | | | | Halloysite, 3 | | | |
| | 118 | 1.244 | | | | Mg-illite, 2 | Phengite, 3 | | | | Halloysite, 3 | | | |
| | 119 | 1.183 | | | | K-illite, 3 | Phengite., 2 | | Ferrihyd., 3 | | Halloysite, 3 | | | |
| | 120 | 1.115 | | | | Mg-illite, 3 | | | | | Halloysite, 3 | | Dolomite, 2 | |
| | 121 | 1.289 | | | | | Phengite, 2 | | | | Halloysite, 3 | | | |
| | 122 | 1.104 | | | | K-illite, 3 | | | | | Halloysite, 3 | | | |
| | 123 | 0.795 | | | | K-illite, 2 | Vermiculite, 2 | | Hematite, 3 | | | | | |
| | 124 | 1.102 | | | | K-illite, 3 | | | | | Halloysite, 3 | | | |
| | 125 | | | | | | | | Hematite, 3 | | | | | |
| | 126 | | | | | | | | Hematite, 3 | | | | | |
| 5 | 127 | 1.334 | 1.159 | | | | Muscovite, 3 | | Hematite, 3 | | Halloysite, 3 | | | |
| | 128 | 1.003 | | | | K-illite, 2 | | | Hematite, 3 | | | | | |
| | 129 | 1.305 | | | | | Muscovite, 2 | | Hematite, 3 | | Halloysite, 3 | | | |
| | 130 | 1.244 | | | | | Muscovite, 3 | | Hematite, 3 | | Halloysite, 3 | | | |
| | 131 | 1.505 | | | | | Muscovite, 3 | | Hematite, 3 | | Halloysite, 3 | | | |
| | 132 | 0.987 | | | | | Phengite, 2 | | | | Halloysite, 3 | | Dolomite, 2 | |
| 6 | 133 | 0.765 | 0.794 | Fe-Sapo., 2 | | K-illite, 3 | | | Hematite, 3 | | | | | |
| | 134 | 0.823 | | | | Mg-illite, 3 | | | Goethite, 3 | | KaoliniteWX, 2 | | | |
| 7 | 135 | 1.077 | 1.11 | | | Mg-illite, 3 | | | Hematite, 3 | | Halloysite, 3 | | Dolomite, 2 | |
| | 136 | 1.143 | | | | | Phengite, 2 | | Hematite, 3 | | Halloysite, 3 | | Dolomite, 2 | |

Table 4. Pie charts of full mineral group detections for Cotter Mine.

| Zone | Minerals Detected | Smectite | Illite | Mica | FeOxide | Kaolinite | Evaporite | Carbonate | Epidote | SUM (n) |
|---|---|---|---|---|---|---|---|---|---|---|
| 1 | 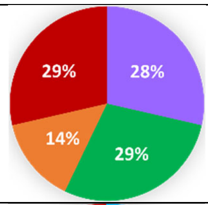 | 0 | 2 | 1 | 2 | 2 | 0 | 0 | 0 | 7 |
| 2 | 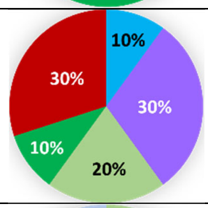 | 2 | 1 | 0 | 3 | 3 | 2 | 0 | 0 | 10 |
| 3 | 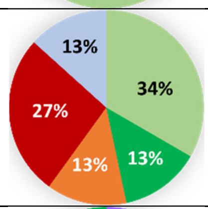 | 5 | 2 | 2 | 4 | 0 | 2 | 0 | 0 | 15 |
| 4 | 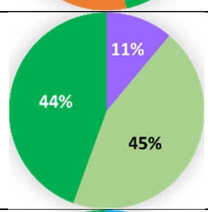 | 4 | 4 | 0 | 0 | 1 | 0 | 0 | 0 | 9 |
| 5 | 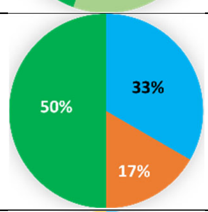 | 1 | 3 | 0 | 0 | 0 | 0 | 2 | 0 | 6 |
| 6 | 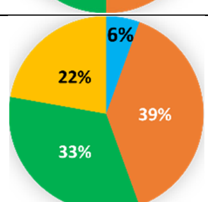 | 7 | 6 | 0 | 0 | 0 | 0 | 1 | 4 | 18 |
| 7 | 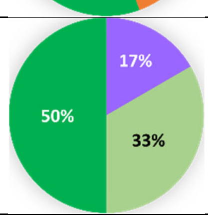 | 2 | 3 | 0 | 0 | 1 | 0 | 0 | 0 | 6 |

Table 5. Detailed Mineral Detections for Cotter Mine. Minerals listed are followed by their star rating. Abbreviations of minerals are: Montmorillonite (Mont.); Beidellite (Beid.). ISM reported for Sample ID 92 is not included in the ISM Average of Zone 5.

| Zone | ID # | ISM | AVG ISM | Smectite | | Illite | Mica | Fe Oxide | Kaolinite | Evaporite | Carbonates | Epidote | Malachite |
|---|---|---|---|---|---|---|---|---|---|---|---|---|---|
| 1 | 72 | 1.166 | 1.492 | | | Mg-illite, 2 | Phengite, 3 | | Halloysite, 3 | | | | |
| | 73 | 1.818 | | | | Mg-illite, 2 | | Goethite, 3 | KaolinitePX, 3 | | | | |
| | 74 | | | | | | | Hematite, 3 | | | | | |
| 2 | 75 | 0.806 | 0.781 | | | | | Hematite, 3 | Halloysite, 2 | | | | |
| | 76 | 0.755 | | | | K-illite, 2 | | | KaolinitePX, 2 | | | | |
| | 77 | | | Mont., 3 | | | | Goethite, 3 | | | Calcite, 3 | | |
| | 78 | | | Mont., 3 | | | | Hematite, 3 | KaolinitePX, 2 | | | | |
| 3 | 79 | 0.449 | 0.453 | Mont., 3 | | Mg-illite, 2 | | Hematite, 3 | | | | | |
| | 80 | | | Mont., 3 | | | | Hematite, 3 | | | | | |
| | 81 | 0.457 | | Mont., 3 | | Mg-illite, 2 | | Hematite, 2 | | | | | |
| | 82 | 0.457 | | Mont., 3 | | | Phengite, 3 | Ferrihydrite, 3 | | Gypsum, 2 | | | |
| | 83 | 0.449 | | Mont., 3 | | | Phengite, 2 | | | Gypsum, 3 | | | |
| 4 | 84 | 0.548 | 0.640 | Mont., 3 | Nontronite, 2 | Mg-illite, 3 | | | | | | | |
| | 85 | 0.667 | | Mont., 3 | | Mg-illite, 3 | | | | | | | |
| | 86 | 0.587 | | Mont., 3 | | Mg-illite, 3 | | | | | | | |
| | 87 | 0.758 | | | | Mg-illite, 3 | | | Halloysite, 3 | | | | |
| 5 | 92 | 2.843 | 0.490 | | | Mg-illite, 3 | | | | | | | Malachite, 3 |
| | 93 | 0.484 | | | | Mg-illite, 2 | | | | | Calcite, 2 | | |
| | 94 | 0.484 | | | | Mg-illite, 2 | | | | | Calcite, 2 | | |
| | 95 | 0.502 | | Mont., 3 | | Mg-illite, 3 | | | | | | | |
| 6 | 88 | 0.502 | 0.471 | Mont., 3 | | Mg-illite, 3 | | | | | Calcite, 2 | | |
| | 89 | 0.462 | | Mont., 3 | | Mg-illite, 3 | | | | | | Epidote, 2 | |
| | 90 | 0.477 | | Mont., 3 | Rectorite, 2 | Mg-illite, 3 | | | | | | | |
| | 91 | 0.501 | | Mont., 3 | | Mg-illite, 3 | | | | | | Epidote, 2 | |
| | 96 | 0.44 | | Mont., 3 | | Mg-illite, 3 | | | | | | Epidote, 2 | |
| | 97 | 0.443 | | Mont., 3 | | Mg-illite, 3 | | | | | | Epidote, 2 | |
| 7 | 98 | 0.752 | 0.658 | | | Mg-illite, 3 | | | Halloysite, 3 | | | | |
| | 99 | 0.649 | | Beid., 3 | | Mg-illite, 3 | | | | | | | |
| | 100 | 0.572 | | Beid., 3 | | Mg-illite, 3 | | | | | | | |

Table 6. Pie charts of full mineral group detections for Prospect Pit.

| Zone | Minerals Detected | Smectite | Illite | Mica | FeOxide | Kaolinite | Evaporite | SUM (n) |
|---|---|---|---|---|---|---|---|---|
| 1 | 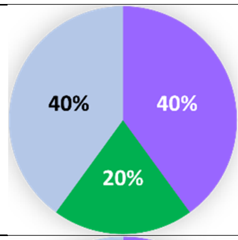  | 0 | 1 | 0 | 0 | 2 | 2 | 5 |
| 2 | 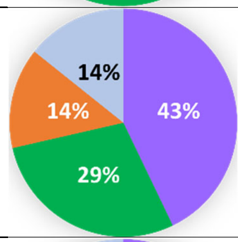  | 0 | 2 | 1 | 0 | 3 | 1 | 7 |
| 3 | 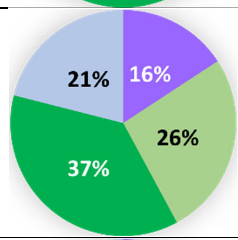  | 5 | 7 | 0 | 0 | 3 | 4 | 19 |
| 4 | 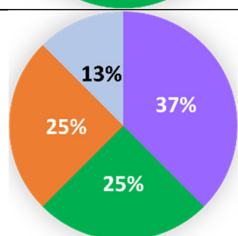  | 0 | 2 | 2 | 0 | 3 | 2 | 8 |
| 5 | 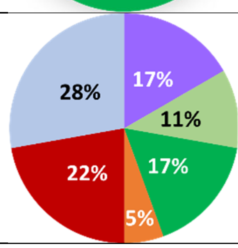  | 2 | 3 | 1 | 4 | 3 | 5 | 18 |

Table 7. Detailed Mineral Detections for Prospect Pit. Minerals listed are followed by their star rating. Sample 57 was scanned where the Malachite star is in Figure 11a, where no was ISM reported and therefore not included in a zone ribbon of Figure 11b.

| Zone | ID # | ISM | AVG ISM | Smectite | | Illite | Mica | Fe Oxide | Kaolinite | Evaporite | Malachite |
|---|---|---|---|---|---|---|---|---|---|---|---|
| 1 | 60 | 0.844 | 0.826 | | | | | | KaolinitePX, 3 | Gypsum, 2 | |
| | 61 | 0.807 | | | | Mg-illite, 3 | | | KaolinitePX, 3 | Gypsum, 2 | |
| 2 | 58 | 0.99 | 1.082 | | | K-illite, 3 | | | KaolinitePX, 2 | | |
| | 59 | 1.127 | | | | Mg-illite, 3 | | | Halloysite, 3 | | |
| | 67 | 1.13 | | | | | Phengite, 3 | | Halloysite, 3 | Gypsum, 2 | |
| 3 | 54 | 0.647 | 0.692 | Montmorillonite, 3 | Nontronite, 2 | Mg-illite, 3 | | | | | |
| | 56 | 0.677 | | Beidellite, 3 | | Mg-illite, 3 | | | | Gypsum, 2 | |
| | 62 | 0.689 | | Beidellite, 3 | | Mg-illite, 3 | | | | Gypsum, 2 | |
| | 63 | 0.642 | | Beidellite, 3 | | Mg-illite, 3 | | | | Gypsum, 3 | |
| | 64 | 0.841 | | | | Mg-illite, 3 | | | KaoliniteWX, 3 | | |
| | 65 | 0.754 | | | | Mg-illite, 3 | | | Halloysite, 3 | | |
| | 66 | 0.591 | | | | Mg-illite, 3 | | | | Gypsum, 3 | |
| 4 | 52 | 1.105 | 1.129 | | | Mg-illite, 2 | Phengite, 3 | | Halloysite, 3 | | |
| | 53 | 0.919 | | | | Mg-illite, 3 | | | KaoliniteWX, 3 | Gypsum, 2 | |
| | 55 | 1.364 | | | | | Phengite, 3 | | Halloysite, 3 | | |
| 5 | 49 | 0.443 | 0.596 | | | | | Goethite, 3 | Halloysite, 3 | Gypsum, 3 | |
| | 50 | 0.636 | | | | | | Goethite, 2 | KaolinitePX, 2 | Gypsum, 2 | |
| | 51 | 0.66 | | Beidellite, 3 | | Mg-illite, 3 | | | | | |
| | 68 | 0.462 | | | | Mg-illite, 2 | | Hematite, 3 | | Gypsum, 2 | |
| | 69 | 0.614 | | | | Mg-illite, 3 | | Hematite, 3 | KaolinitePX, 2 | Gypsum, 3 | |
| | 70 | 0.763 | | Montmorillonite, 3 | | | Phengite, 3 | | | Gypsum, 2 | |
| -- | 57 | | | | | | | Goethite, 3 | KaoliniteWX, 3 | Gypsum, 2 | Malachite, 3 |

## REFERENCES


Bailey, L. R., Kirk, J., Hemming, S. R., Krantz, R. W., & Reiners, P. W. (2021). Eocene fault-controlled fluid flow and mineralization in the Paradox Basin, United States. *Geology*, *50*(1). https://doi.org/10.1130/g49466.1

Barton, M. D., Barton, I. F., & Thorson, J. P. (2018). Paleofluid Flow in the Paradox Basin : Introduction. In *Paradox Basin Fluids and Colorado Plateau Copper, Uranium, and Vanadium Deposits Field Trip; Guidebook Series* (Vol. 59, pp. 1–12).

Bergman, S. C., Huntington, K. W., & Crider, J. G. (2013). Tracing paleofluid sources using clumped isotope thermometry of diagenetic cements along the moab fault, Utah. *American Journal of Science*, *313*, 490–515. https://doi.org/10.2475/05.2013.03

Caine, J. S., Evans, J. P., & Forster, C. B. (1996). Fault zone architecture and permeability structure. *Geology*, *24*(11), 1025–1028. https://pubs.geoscienceworld.org/gsa/geology/article-pdf/24/11/1025/3516124/i0091-7613-24-11-1025.pdf

Chan, M. A., Parry, W. T., & Bowman, J. R. (2000). Diagenetic hematite and manganese oxides and fault-related fluid flow in Jurassic sandstones, Southeastern Utah. *AAPG Bulletin*, *84*(9), 1281–1310. https://doi.org/10.1306/A9673E82-1738-11D7-8645000102C1865D

Chan, Marjorie A., Parry, W. T., Petersen, E. U., & Hall, C. M. (2001). 40Ar/39Ar age and chemistry of manganese mineralization in the Moab and Lisbon fault systems, southeastern Utah. *Geology*, *29*(4), 331–334. https://doi.org/10.1130/0091-7613(2001)029<0331:AAAACO>2.0.CO;2

Condon, S. M. (1997). Geology of the Pennsylvanian and Permian Cutler Group and Permian Kaibab Limestone in the Paradox Basin, Southeastern Utah and Southwestern Colorado. *Evolution of Sedimentary Basins Paradox Basin*, *U.S. Geological Survey Bulletin 2000-P*.

Davatzes, N C, & Aydin, A. (2005). Distribution and Nature of Fault Architecture in a Layered Sandstone and Shale Sequence: An Example from the Moab Fault, Utah. *AAPG Memoir*, *85*, 153–180. https://doi.org/10.1306/1033722M853134

Davatzes, Nicholas C., Aydin, A., & Eichhubl, P. (2003). Overprinting faulting mechanisms during the development of multiple fault sets in sandstone, Chimney Rock fault array, Utah, USA. *Tectonophysics*, *363*(1–2), 1–18. https://doi.org/10.1016/S0040-1951(02)00647-9

Davidson, I., Alsop, I., & Blundell, D. (1996). Salt tectonics: Some aspects of deformation mechanics. *Geological Society Special Publication*, *100*(100), 1–10. https://doi.org/10.1144/GSL.SP.1996.100.01.01

Doelling, H. H. (1988). *Salt Deformation in the Paradox Region, Utah* (Bulletin 1). Utah Geological and Mineral Survey.

Doelling, H. H., & Baars, D. L. (1987). Moab salt-intruded anticline, east-central Utah. *Rocky Mountain Section of the Geological Society of America*, 275–280. https://doi.org/10.1130/0-8137-5402-x.275

Doelling, Hellmut H. (1985). *Geology of Arches National Park*.

Doelling, Hellmut H., & Morgan, C. D. (2000). *Geologic Map of the Merrimac Butte*.

Doublier, M. P., Roache, T., & Potel, S. (2010). Short-wavelength infrared spectroscopy: A new petrological tool in low-grade to very low-grade pelites. *Geology*, *38*(11), 1031–1034. https://doi.org/10.1130/G31272.1

Eichhubl, P., Davatzes, N. C., & Becker, S. P. (2009). Structural and diagenetic control of fluid migration and cementation along the Moab fault, Utah. *AAPG Bulletin*, *93*(5), 653–681. https://doi.org/10.1306/02180908080

Fillmore, R. (2011). Geological Evolution of the Colorado Plateau of Eastern Utah and Western Colorado. *The University of Utah Press.*

Foxford, K. A., Garden, R., Guscott, S. C., Burley, S. D., Lewis, J. J. M., Walsh, J. J., & Watterson, J. (1996). *The Field Geology of the Moab Fault* (L. H. Godwin, A. C. Huffman, & W. R. Lund (eds.)). Utah Geological Association.

Foxford, K. A., Walsh, J. J., Watterson, J., Garden, I. R., Guscott, S. C., & Burley, S. D. (1998). Structure and content of the Moab Fault Zone, Utah, USA, and its implications for fault seal prediction. *Geological Society Special Publication*, *147*(November 2017), 87–103. https://doi.org/10.1144/GSL.SP.1998.147.01.06

Gard, L. M. (1976). Geology of the North End of the Salt Valley Anticline, Grand County. In *United States Department of the Interior Geological Survey*.

Garden, I. R., Guscott, S. C., Burley, S. D., Foxford, K. A., Walsh, J. J., & Marshall, J. (2001). An exhumed palaeo-hydrocarbon migration fairway in a faulted carrier system, Entrada Sandstone of SE Utah, USA. *Geofluids*, *1*, 195–213. https://doi.org/10.1046/j.1468-8123.2001.00018.x

Haines, S. H., & van der Pluijm, B. A. (2012). Patterns of mineral transformations in clay gouge, with examples from low-angle normal fault rocks in the western USA. In *Journal of Structural Geology* (pp. 2–32). https://doi.org/10.1016/j.jsg.2012.05.004

Haines, S. H., Van Der Pluijm, B. A., Ikari, M. J., Saffer, D. M., & Marone, C. (2009). Clay fabric intensity in natural and artificial fault gouges: Implications for brittle fault zone processes and sedimentary basin clay fabric evolution. *Journal of Geophysical Research: Solid Earth*, *114*(B05406), 1–22. https://doi.org/10.1029/2008JB005866

Johansen, T. E. S., & Fossen, H. (2008). Internal geometry of fault damage zones in interbedded siliciclastic sediments. *Geological Society Special Publication*, *299*, 35–56. https://doi.org/10.1144/SP299.3

Johansen, T. E. S., Fossen, H., & Kluge, R. (2005). The impact of syn-faulting porosity reduction on damage zone architecture in porous sandstone: An outcrop example from the Moab Fault, Utah. *Journal of Structural Geology*, *27*(8), 1469–1485. https://doi.org/10.1016/j.jsg.2005.01.014

Malvern Panlytical. (2018). *TerraSpec Halo User Manual*. Malvern Panalytical.

Nuccio, V. F., & Condon, S. M. (1996). Burial and Thermal History of the Paradox Basin, Utah and Colorado, and Petroleum Potential of the Middle Pennsylvanian Paradox Formation. In *U.S. Geologicial Survey Bulletin 2000*.

Pevear, D. R. (1999). Illite and hydrocarbon exploration. *Proceedings of the National Academy of Sciences*, *96*, 3440–3446. https://doi.org/10.1073/pnas.96.7.3440

Pevear, D. R., Vrolijk, P. J., & Longstaffe, F. J. (1997). Timing of Moab Fault Displacement and Fluid Movements Integrated with Burial History using Radiogenic and Stable Isotopes. *Contributions to the Second International Conference on Fluid Evolution, Migration and Interaction in Sedimentary Basins and Orogenic Belts: Geofluids II Conference, The Queen's University of Belfast, Belfast, Northern Ireland, Geofluids II Extended Abstr*, 42–45.

Solum, J. G., Davatzes, N. C., & Lockner, D. A. (2010). Fault-related clay authigenesis along the Moab Fault: Implications for calculations of fault rock composition and mechanical and hydrologic fault zone properties. *Journal of Structural Geology*, *32*, 1899–1911. https://doi.org/10.1016/j.jsg.2010.07.009

Solum, J. G., van der Pluijm, B. A., & Peacor, D. R. (2005). Neocrystallization, fabrics and age of clay minerals from an exposure of the Moab Fault, Utah. *Journal of Structural Geology*, *27*, 1563–1576. https://doi.org/10.1016/j.jsg.2005.05.002

Turner, C. E., & Fishman I Ge, N. S. (1991). Jurassic Lake T'oo'dichi': A large alkaline, saline lake, Morrison Formation, eastern Colorado Plateau. *Geological Society of America Bulletin*, *103*, 538–558. http://pubs.geoscienceworld.org/gsa/gsabulletin/article-pdf/103/4/538/3381313/i0016-7606-103-4-538.pdf

Vrolijk, P., & Van Der Pluijm, B. A. (1999). Clay gouge. *Journal of Structural Geology*, *21*, 1039–1048. https://doi.org/10.1016/S0191-8141(99)00103-0

Whitehead, A. (2019). *Comparison of Sediment-Hosted Cu Mineralization Lisbon and Moab Fault Systems, Utah* [Univeristy of Arizona]. http://hdl.handle.net/10150/634336

## BIOGRAPHICAL SKETCH

Paula Fleischmann was born in Afula, Israel. After graduating from Allen High School, she went on to get her first Bachelor of Science degree at The University of Texas at Dallas, graduating in 2016. Paula was then employed at GeoFrontiers Corp. in Rowlett, Texas as a laboratory technician. In August of 2017, she returned to The University of Texas at Dallas where she received a Master of Science in Geoscience in May 2022. During her time as a graduate student, she was a teaching assistant for two semesters for the Environmental Geology course, served as the President of the American Association of Petroleum Geologists (AAPG) Student Chapter at UT Dallas, attended and presented at conferences (AAPG and Geological Society of America), and competed in the 2020 Imperial Barrel Award competition held by AAPG where together, she and her team won 1st Place at Southwest Section and competed in the global competition representing the UT Dallas Geosciences Department. She continues to be employed in the oil and gas industry at GeoFrontiers Corp.

# CURRICULUM VITAE

## PAULA FLEISCHMANN

**Education**

Master of Science (MS) in Geosciences
The University of Texas at Dallas
Fall 2017 – Spring 2022

Bachelor of Science (BS) in Geosciences
The University of Texas at Dallas
Fall 2010 – Summer 2016

**Professional Experience**

Laboratory Technician, GeoFrontiers Corp., Rowlett, TX
Feb 2017 – Present

**TA Experience**

Course: Environmental Geology, Fall 2019 – Spring 2020
Instructor: Dr. Thomas Brikowski

**Field Work Experience**

GeoFrontiers Corp.
July 2021 and August 2021
Location: Montague County, TX
Solid-Phase Microextraction Soil Absorber Sampling

University of Texas at Dallas, Department of Geosciences
September 2018, May-June 2019
Location: Moab, UT
MS Thesis Project: Infrared data and physical sample collection

University of Texas at Dallas, Department of Geosciences
Summer 2015, Summer 2016
Locations: San Ysidro, NM, Baca Canyon, NM, Gardner, CO (2015); Dyer, NV (2016)
Field Camp courses I & II for BS Degree

**Conference Presentations**

American Association of Petroleum Geologists, 2020 Annual Conference and Exhibition
Poster Presentation: *"Assessing Fault Seal Behavior Using Fluid Flow Indicators from Infrared Spectral Measurements of Clay Gouge in the Moab Fault, Utah"*

Geological Society of America, 2019 Annual Conference, Phoenix, AZ
Oral Presentation: "*Using Infrared Spectroscopy to Assess Paleofluid Flow Characteristics of Clay Gouge of The Moab Fault, UT"*

**Leadership Experience**

AAPG at UT Dallas Student Chapter
President, May 2019 – May 2020
Treasurer, May 2018 – May 2019 and May 2020 – May 2021

UTD Geoclub
President, August 2015 – May 2016

Alpha Gamma Delta: 2010 – 2014
VP Recruitment, January 2011 – November 2011

**Skills**

Malvern Panlytical Terraspec Halo, Petrel, ArcGIS and ArcMap, Adobe Illustrator, Microsoft Excel, Unreal Tournament

**Awards, Honors, Special Recognition**

Imperial Barrel Award Competition 2020, Hosted by AAPG:
1st Place Southwest Section and Global Finalist Participant

Kristian Soegaard Memorial Scholarship 2016

UTD Geoclub: Nomination for Golden Comet Award 2016

Alpha Gamma Delta, Epsilon Psi Chapter: Most Outstanding New Member Award 2010

**Professional Memberships**

American Association of Petroleum Geologists (AAPG), Student Member
American Institute of Professional Geologists (AIPG), Student Member
Geological Society of America (GSA), Student Member
Dallas Geological Society (DGS), Student Member